Solar Energy 294 (2025) 113516

Contents lists available at ScienceDirect

Solar Energy

journal homepage: www.elsevier.com/locate/solener

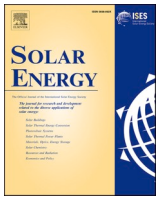

Very short-term solar irradiance forecasting based on open-source low-cost sky imager and hybrid deep-learning techniques

Martin Ansong [a,b], Gan Huang [a], Thomas N. Nyang'onda [b], Robinson J. Musembi [b], Bryce S. Richards [a,c,*]

[a] Institute of Microstructure Technology, Karlsruhe Institute of Technology, Hermann-von-Helmholtz-Platz 1, 76344 Eggenstein-Leopoldshafen, Germany
[b] Department of Physics, University of Nairobi, Nairobi 30197-00100, Kenya
[c] Light Technology Institute, Karlsruhe Institute of Technology, Engesserstrasse 13, 76131 Karlsruhe, Germany

ARTICLE INFO

Keywords:
Low-cost sky imager
Solar irradiance
Short-term forecasting
Deep learning
CNN-LSTM
Cloud fraction

ABSTRACT

Solar irradiance (SI) forecasting is vital for reliable photovoltaic (PV) operation. This is especially true for regions like Africa where many SI forecasting approaches rely on scarce historical data and the inherent instabilities of electric grids are further compounded by SI variability. Accurate solar forecasting is essential for improving grid management, enabling operators to balance supply and demand and enhance stability. Ground-based sky imaging is a promising technique for SI forecasting that do not require extensive historical data. However, commercial sky imagers are expensive and offer limited flexibility. This paper introduces the Karlsruhe low-cost all-sky imager (KALiSI), made from off-the-shelf components that captures high-resolution images and can be assembled for less than €600. The KALiSI was installed in Karlsruhe, Germany, to collect images to train a convolution neural network-long short-term memory (CNN-LSTM) model for 15 min-ahead forecasting of global horizontal irradiance (GHI). The root mean squared (RMS) error of the model ranges from 19–206 W/m^2, compared to 33–257 W/m^2 for persistence, while mean absolute (MA) errors range from 15–144 W/m^2 for CNN-LSTM and 30–159 W/m^2 for persistence. The model's performance using KALiSI's images was compared with a commercial sky imager at the same location across various forecast horizons. The KALiSI showed normalised RMS error and MA error values of 6 % and 7 % higher, respectively, with some discrepancies noted on clear days. These results show the KALiSI's suitability for very short-term forecasting and its open-source design offers a low-cost solution for developing countries.

1. Introduction

Solar energy is regarded as a key alternative to meet the rising global energy demands and replace conventional fossil-fuel energy generation systems [1]. In order to ensure the effective and efficient utilisation of solar energy technologies, for example, for photovoltaic (PV) power generation, it is of the utmost importance to gain a comprehensive understanding of the solar resource potential across a wide range of geographic locations. A lot of effort has been put into analysing historical data and making yearly, monthly, daily and even hourly solar irradiance (SI) datasets available, a classic example of this being Photovoltaic Geographical Information System (PVGIS) [2]. Such solar resource assessment tools are indispensable for the effective design, sizing, operation, and positioning of PV systems. PV power is environmentally friendly, secure, sustainable, and is currently the fastest growing renewable electricity source by capacity additions with its installed grid-connected capacity surpassing that of wind energy in 2023 [3]. It accounted for nearly 75 % of all renewable power additions in 2023 and in terms of electricity generation it currently ranks third (after wind and hydropower) and is projected to be second only to hydropower by 2028 [1,3]. The PV market has been experiencing rapid expansion [4], with PV power generation, transmission, maintenance, and utilisation becoming integral elements in the establishment of smart grid systems [5].

Nevertheless, solar energy is variable and its availability changes depending on diverse weather conditions, including sunlight intensity, cloud cover, temperature variations, and relative humidity levels [6,7]. Such fluctuations and periods of intermittency result in uncertainties and inefficiencies in the operation of PV power systems [8]. The integration of PV power into existing grids poses significant challenges to

* Corresponding author.
E-mail address: bryce.richards@kit.edu (B.S. Richards).

https://doi.org/10.1016/j.solener.2025.113516
Received 5 November 2024; Received in revised form 4 April 2025; Accepted 10 April 2025
Available online 16 April 2025

Table 1
Solar irradiance forecasting approaches summarised from the literature, including the root mean squared (RMS) error compared to the intensity of standard terrestrial sunlight (1000 W/m^2).

Forecastapproach	Forecast horizon	Data required	Spatial resolution	Typical applications	Accuracy (RMS error)	Refs.
Time series analysis	Up to 6 h	Historical data	1−2 km	Load following	up to 100 W/m^2	[19–21]
NWP models	3 h−10 d	Historical data, meteorological parameters	5−20 km	Unit commitment, scheduling	400 W/m^2	[19–24]
Satellite imagery	30 min−6h	Satellite images	1−10 km	Load following	60–350 W/m^2	[20–22,24]
Sky imagery	up to 30 min	Ground-based sky images, historical data (optional)	1−2 km	Short-term ramps, stability, regulation	6–9 % normalised	[19–22]
Hybrid models	Up to 15 d	Historical data, meteorological data, Satellite images	1−20 km	Regulation, load following, unit commitment, scheduling,	up to 100 W/m^2	[20–22]

the stability and security of the electricity infrastructure. Consequently, SI forecasting is key to improving the stability and reliability of PV power generation. Knowing in advance what SI, and therefore the amount solar power, will be in the next few minutes can help utilities make informed decisions about power dispatch, power management, energy planning, power sales and pricing, and energy storage control [8,9]. The accuracy of the forecast also has an impact on the financial aspects of solar farms [6,7]. In developing regions such as Africa, many weak power grids exist and usually coincide with the availability of vast solar resources. In such cases, accurate SI prediction has the additional value of enabling better load matching, i.e. matching demand to supply, thus creating more robust electricity grids [10,11].

There are several approaches to SI forecasting, each offering different levels of accuracy, having different requirements, and operating over different forecast horizons. These include time series analysis/statistical methods, numerical weather prediction (NWP) models, ground-based sky observations, satellite imagery, as well as hybrid methods that combine two or more of the above approaches. Most of these SI forecasting approaches rely heavily on the existence of historical data and also tend to provide long-term forecasts, typically a few hours to several days ahead, as summarised in Table 1. However, this historical data is lacking in many developing countries, especially in Africa, which in turn hampers economic development [12,13]. A promising technology that may not require many years of historical data and is being explored for solar resource assessment and forecasting is ground-based sky imaging systems that are used for remote sensing of clouds [14–18].

1.1. Sky image-based solar irradiance forecasting

Ground-based sky imaging techniques for cloud analysis and atmospheric studies mostly use upward-facing cameras equipped with a fish-eye lens or cameras pointing downwards on a hemispherical mirror to capture the entire visual sky [25,26]. Most of these cameras capture images in red–green–blue (RGB) format, where the intensities of the three channels can be separated for further sky analysis [26–28]. When combined with advanced image processing, the images from these cameras can be used to predict the incoming SI by determining the amount of cloud cover and analysing the distribution, movement and optical properties of clouds. SI forecasting with these images typically involves the extraction of features such as red-blue ratio (R:B), cloud cover, and cloud motion vectors to construct deterministic physical models [14,17,29] or to train machine learning (ML) models for SI prediction [30–32].

Sky imaging techniques usually operate over very short time horizons (up to 30 min) [20,33] in contrast to satellite imagery, NWP and time series analysis/statistical methods, which are all more focused on long-term prediction and typically over large areas. A method combining sky imagery and real-time SI measurements has been used to predict 1-min. averaged SI up to 10 min in advance [31]. The reported minimum and maximum RMS errors for the days selected for testing are less than 6 W/m^2, 184–251 W/m^2 and 64–110 W/m^2 for clear, cloudy and overcast sky conditions, respectively. Another method combined sky images with other meteorological parameters, such as relative humidity (RH%) and aerosol optical depth (AOD) at 500 nm, as input to an LSTM network with Bayesian optimisation, to predict the GHI 10 min in advance. The model achieved a normalised RMS error of ~15 % under all sky conditions [34]. Tiwari et al. [35] also proposed a short-term SI prediction framework using sky images and a residual learning algorithm (ResNet50) to predict the corresponding SI value for the next 10 min. The reported RMS error between the actual and predicted values of SI for three selected sample days (a clear sky day, a partly cloudy sky day and an overcast day) were 6, 15 and 8 W/m^2, respectively. An LSTM algorithm was used to predict cloud cover 10 min in advance from sky images [36]. The predicted cloud cover data were used to estimate the GHI. The proposed model showed relative RMS differences between 25 and 40 %. Al-lahham et al. [30] used dimensionality reduction techniques to extract features from sky images for short-term SI prediction. Two ML algorithms, random forest (RF) and K-nearest neighbours (KNN), were used to predict SI up to 4 h ahead. KNN achieved the best performance with an hourly prediction RMS error between 116 and 122 W/m^2. The approach achieved competitive results with much less computational complexity compared to other computationally intensive algorithms.

While conventional methods have been mostly used for this purpose, there is a growing interest in using deep learning (DL) techniques for SI prediction from sky images [37–42]. Despite certain limitations, DL models have demonstrated superior predictive performance in SI prediction compared to traditional methods. A long short-term memory (LSTM) model has been employed to predict the solar power 1-min-ahead from a 2.5 kWp PV system using sky images as the model input. The model achieved a 21 % RMS error skill score over persistence and outperformed multi-layer perceptron (MLP), and convolutional neural network (CNN) which achieved 7 % and 12 % RMS error skill scores respectively over persistence [39]. SUNSET, a specialised CNN model, which uses minutely-averaged historical PV power values along with corresponding sequence of sky images as inputs to forecast the 15-min-ahead PV output power has been proposed. The model achieved an overall forecast skill of 16 % relative to the smart persistence forecast under all weather conditions [43]. Another LSTM model was employed to predict GHI from sky images as well as local and external meteorological data – including ambient temperature, GHI, and RH% – over a forecast horizon of 0–20 min. The model achieved an average RMSE 59 and 77 W/m^2 in sunny and partially cloudy weather conditions, respectively, over all prediction horizons [40]. Feng et al. [44], also developed the SolarNet, a 20-layer CNN model, to forecast GHI for time horizons ranging from 10 to 60 min, with 10-min intervals. SolarNet uses a single sky image as input, without relying on any numerical data or additional features. Testing the model with six years of publicly available data demonstrated that SolarNet achieved multi-step forecasts with a normalised RMS error of 9 % and a forecasting skill score of 25 %, significantly outperforming the persistence and a collection of 6 ML

models – two artificial neural networks with different back-propagation, three gradient boosting machines with different loss functions, and random forest model.

1.2. Sky imaging systems

Regarding the equipment, a number of sky imagers have been developed for both commercial and research purposes. Examples include total sky imagers (models TSI-880 and TSI-440, Yankee Environmental Systems, U.S.A.) [45,46] and the ASI-16 from EKO Instruments (built by CMS Shredder, Austria). The total sky imagers are the most widely used systems with a proven track record of reliability in atmospheric studies [45]. The ASI-16 with a higher resolution has extensively been used in weather monitoring, particularly allowing accurate cloud detection and classification, cloud base height determination and SI forecasting [46,47]. Commercially available sky imagers are generally expensive, with prices ranging from €10,000 to €35,000, depending on the manufacturer, model and sophistication. Such systems mostly use low-resolution image sensors and come with proprietary software packages, offering very limited flexibility, thus making customisation difficult or even impossible [48]. These factors have motivated some researchers to develop versions of sky imagers targeting specific research needs.

The University of California, San Diego, in collaboration with Panasonic Ltd., designed and developed a high dynamic range (HDR) sky imager system for the specific purpose of short-term solar power forecasting applications [15]. This sky imager is capable of capturing the entire hemisphere of the sky using an upward-facing charge-coupled device (CCD) image sensor and a fisheye lens at a rate of every 1.3 s [45]. However, there are several disadvantages: i) the raw images captured by the camera are not well-suited for visual inspection on a user's screen because they are in raw Bayer format (not in colour); ii) the large file sizes (e.g. 3 MB per image resulting in 3 and 6 GB per day for daylight hours depending on time of year) result in slow loading; and iii) much of the sky falls within the lower range of the 16-bit dynamic range, causing the image to appear very dark except for the sun [45].

Kazantzidis et al. [49] also developed a sky imager utilising a commercial compact digital camera (Canon IXUS II) and a fisheye lens (field of view = 180°). The system is encased in a water and weather-resistant box with a glass dome, devoid of any mechanism for obscuring the direct solar radiation. The camera was connected to a personal computer to allow external automated control. It was programmed to acquire 8-bit JPEG format images with spatial resolution of 640 × 480 pixels every 5 min for the purpose of automatic estimation of total cloud coverage and classification of clouds. The classifier was able to detect seven cloud types with accuracy of 78 to 95 % and average performance of 88 %.

The wide-angle high-resolution sky imaging system (WAHRSIS), designed and constructed by Dev et al. [48], has an estimated cost of €2300. This sky imager is capable of capturing light across the visible and near-infrared spectral ranges. The WAHRSIS was constructed using off-the-shelf components, including a Canon digital camera, a circular fish-eye lens, and an alteration for near-infrared sensitivity. The alteration allows the camera to see through haze conditions and provide sharper images, important when studying the properties of clouds. The initial design included a mechanical sun-blocker for the purpose of reducing glare around the circumsolar region in each captured image. However, in addition to occupying a significant region of the visible sky in each image, the sun-blocker introduced operational problems and ceased to function after extensive use. Consequently, it was removed in later models of the WAHRSIS, making them both smaller and cheaper (< €1700), while HDR imaging techniques were employed to reduce the sun's glare.

Another sky imager was constructed at an estimated cost of €460 for cloud motion prediction and SI forecasting [50]. This employed a single-board computer and a programmable high-resolution camera in a weatherproof enclosure. In addition, the low-cost and miniature ground-based sky camera (LAMSkyCam) has also been developed around a single-board computer at a remarkably low cost of about €300 [51]. This lightweight miniature sky imager with a limited (63°) viewing angle is capable of capturing high-resolution images of the sky at 5-min intervals, both during the day and night. To capture images for night-time cloud analysis, the camera automatically increases the exposure time (shutter speed) to allow more light to the sensor. The lower viewing angle and temporal resolution of the LAMSkyCam limit its suitability for SI forecasting applications. With a restricted field of view, it is unable to capture the full sky, thus missing important cloud formations and movement information. Furthermore, its lower temporal resolution impairs the ability to track fine cloud details and changes in SI over short time intervals, thereby reducing forecast accuracy.

1.3. Motivation

The limitations of commercial sky imagers impede mass deployment and render them impractical in small-scale systems where there may be the need to forecast ramps in power output caused by SI fluctuations. In addition, the accuracies of SI forecasting models remain inadequate, prompting ongoing efforts from researchers to improve them through the application of diverse methodologies. There is a need for low-cost but still robust sky imaging systems that can be used for SI forecasting with hybrid DL techniques. Furthermore, the comparison of the performance of forecasting based on such custom-built low-cost sky imagers and commercial sky imagers is still limited in the literature. These challenges motivated the development of an easy-to-assemble but robust all-sky imager for SI forecasting called the Karlsruhe low-cost all-sky imager (KALiSI), which is presented in this paper. This low-cost sky imager is fabricated from readily available off-the-shelf components. Thanks to the RaspberryPi (RPi) model 4B single-board computer used, the imager has a high computational capability, which results in faster processing, better multitasking capabilities, and improved overall performance compared to similar low-cost imagers in its class. The design is simple, facilitating the assembly of the various components in a timely and straightforward manner (typical construction time ~ 2 days). Also, it is intended to be compact and portable, thus facilitating ease of installation in the field. For applications in short-term SI forecasting, it is necessary to capture sky information in high resolution [52], and this imager has been developed with this in mind. It has a wide field of view and can capture high-resolution images at an interval of 1 min or more. The KALiSI has been used to collect data for very short-term SI forecasting using a hybrid DL approach. To fully evaluate the new design, a comparison is made between the KALiSI and a commercially-available sky imager. First, cloud fraction estimates from both imagers are compared using the same cloud detection algorithm. This step evaluates whether the low-cost imager can reliably capture cloud cover information before being utilised for SI forecasting. Second, the same SI forecasting model is applied to images from both imagers to assess how image quality influences prediction accuracy. This approach helps determine whether the commercial imager offers a significant forecasting advantage over the low-cost alternative.

Importantly, it should also be noted here that all materials, component descriptions, and program codes are made available as open source.[1] With regard to applying DL methods to solar forecasting, this work particularly builds on previous efforts such as those presented in the works of Sun et al. [38,43], which employed CNN models for PV power prediction based on sky images and historical PV power data. It advances these approaches by combining CNN and LSTM in a hybrid model to forecast SI with images captured by a low-cost sky imager and cloud fractions calculated from the images, without relying on historical measurements or additional features. The research addresses three key questions: i) how can a low-cost sky imager be designed for SI

[1] https://github.com/KALiSI4SIFS/KALiSI.git.

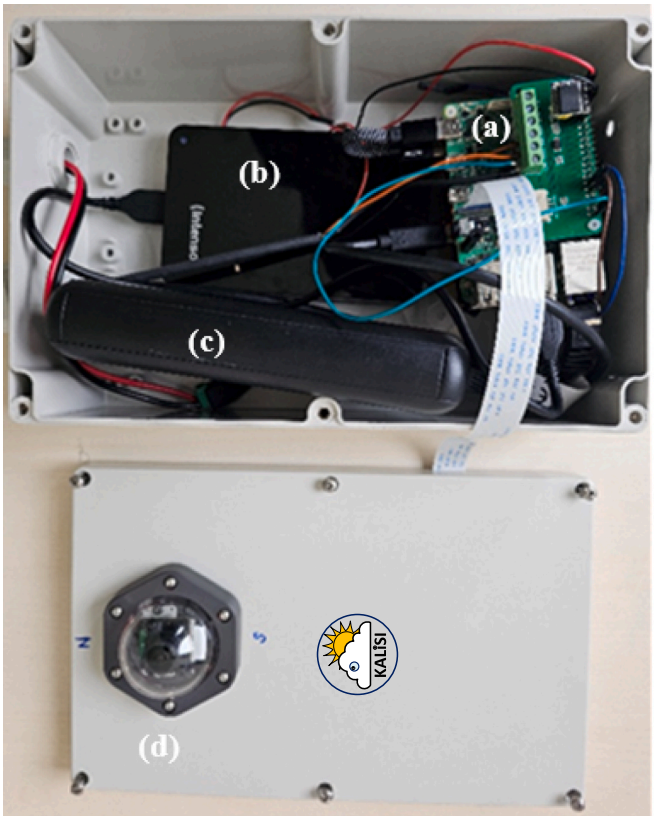

Fig. 1. Weather-resistant enclosure of the KALiSI, housing the (a) RPi with RTC and ADC; (b) the SSD external storage; (c) power-bank as a backup battery; and (d) the camera module secured in the weatherproof dome case mounted on top of the enclosure.

forecasting? ii) how can hybrid machine learning models forecast SI using images from this imager without auxiliary weather data? iii) how does cloud fraction estimates and SI forecasting performance from this custom low-cost imager compare to a commercial system?

2. Materials and methods

2.1. Design and construction of low-cost sky imager

The KALiSI, as illustrated in Fig. 1, is constructed using off-the-shelf components, including a RPi 4 single-board computer (Model B, Raspberry Pi Foundation: Cambridge, UK, 8 GB RAM), which is equipped with a fully programmable, high-resolution RPi camera module (v2, Raspberry Pi Foundation: Cambridge, UK, 8 megapixels). The RPi camera is capable of capturing images with a resolution of 3280 × 2464 pixels with an original viewing angle of 62°. This was significantly enhanced via the implantation of a super-wide angle (220°) fisheye lens (Entaniya RPi camera lens, RP-L 220, Japan). Since the RPi used in the KALiSI does not come with a built-in real-time clock (RTC), an RTC (DS3231) module is added to ensure it does not lose track of the current time when the device is powered off or rebooted. An uninterruptable power supply (PiPower UPS, 5 V/3A, 2000 mAh, SunFounder, China) is also added to ensure that the RPi keeps running in case of a power fluctuation or failure. The components were assembled in a weatherproof plastic enclosure (TRU COMPONENTS, material: ABS, IP-protection: IP65/66, dimension: 250 x 160 x 90 mm) with a water-resistant transparent dome case (Entaniya WC-01, Japan) for the camera. To facilitate portability and ease of use in remote locations – e.g. lacking internet connectivity and an external power source – an external storage device, a power-bank (e.g. Ansmann Powerbank, PB2125 V, 30 Ah) with pass-through functionality and a 4G USB WiFi modem (e.g. ZTE MF79U, China) may be incorporated. It is recommended that the power-bank be charged with a PV module sufficiently sized (e.g. Off-gridtec, ACM156, 50 W, 20 V, China) and buck converter (e.g Bauer Electronics, DC-DC, 50 W, 10A, 8 – 36 V to 5 V, Germany), in order to ensure a continuous supply to the RPi. The PV module is deliberately oversized to allow for significant power derating when operating in very hot climates. Furthermore, since the RPi can only read digital signals, an analogue to digital (ADC) converter module (Seeed studio, ADS1115, 4-Channel, 16-Bit, China) is added to enable the RPi to read analogue signals. With this module, the system can be interfaced with a SI sensor (for GHI) and temperature sensors for better performance analysis. The ADC is a high-precision, low-power converter based on the Texas Instruments ADS1115. It features a programmable gain amplifier, high-resolution conversion, and a configurable input multiplexer that supports two differential or four single-ended inputs, with a sampling rate of 8 to 860 samples per second. It is ideal for portable instrumentation, and offers reliable and efficient analogue signal processing. Finally, a solid-state drive (SSD) of sufficient capacity (250 GB to 1 TB) is needed to accommodate up to 180 days' worth of images (captured at 1-min. intervals). The schematics of the KALiSI are shown in Figs. A1 and A2 in the Appendix. The entire system can be assembled for less than €600. The costs of the main components used are also listed in Table A1 in the Appendix.

The Linux operating system, which is installed on the RPi, is responsible for managing the control of the camera. A custom Python script issues instructions to the camera, prompting it to take pictures and store them in the onboard storage medium, and/or transmit them to a server. A cron job, a Linux command used for scheduling tasks, is tasked to run the Python script every minute from sunrise to sunset. The determination of sunrise and sunset is achieved through the utilisation of the date, time, longitude and latitude of the geographic location as inputs in the Python script. This is important to avoid taking images all night, wasting both power and storage space.

The system was then taken through a series of field trials and necessary corrective actions were carried out to ensure the system was fully operational. Images were sampled at different times of the day to assess clarity, brightness, and exposure levels. Initially, about 300 images were analysed for distortions and overexposure. Nearly all images were overexposed and inconsistent due to the default automatic white balance setting of the image sensor. To address this, camera settings such as exposure time, white balance, and ISO were adjusted to ensure consistency in all subsequent images. Additionally, an exposure fusion technique was integrated into the Python program, capturing three consecutive images at varying exposure times and merging them to generate a HDR image [53,54]. This adjustment was necessary because the complementary metal-oxide semiconductor (CMOS) image sensor in the RPi camera module (Sony IMX219PQ) lacks the dynamic range capacity of the human eye, making images captured in direct sunlight or dark shadows prone to over- or under-exposure, respectively [50]. Furthermore, during this phase, the alignment and field of view of the lens were checked and adjusted. The system was also tested with various power sources, including battery, solar, and mains, to ensure reliable operation in remote areas e [13]. Wi-Fi connectivity and remote access were also verified for stability. The software's automated image capture functionality was assessed by running scheduled scripts at 1-minute intervals over multiple trials, confirming that server uploads and storage processes operated correctly 100 % of the time.

2.2. Working principle

The RPi serves as the heart of the systems, handling image capture and data storage. The camera module, connected via the CSI port, periodically captures images of the sky. The interval for image capture is set in the custom Python script running on the RPi, typically set to capture at 1 min intervals. The RTC module connected through the I2C interface of the RPi ensures accurate timekeeping, even when the system

Fig. 2. Photograph showing the KALiSI mounted on the weather station mast at the KIT Solar Park. The EKO ASI-16 commercial sky imager can also be seen, along with the SI sensor for measuring GHI (for KALiSI) and the dedicated pyranometer (EKO Instruments, MS80HS, Japan) for the EKO sky imager. Several sensors that are not utilised in this work are mounted below the sky imagers: a precipitation sensor (Lufft, WS100, radar sensor, Germany) an additional pyranometer (Kipp & Zonen, SMP12, The Netherlands), and a multi-weather sensor (Thies Clima sensor US, NHTFB, Germany).

is powered off, which is crucial for timestamping each captured image. The captured images are stored on the SSD drive connected through the USB port. SSD provide fast and reliable storage, essential for the large amount of image data that accumulates over time. The optional ADC module is included to integrate analog weather sensors like temperature, humidity, or SI sensors. These sensors provide real-time weather data, which can be logged alongside the images. The ADC converts the analog signals from the sensors into digital data, which is read by the RPi over the I2C bus. The entire system can be powered by a 5 V power supply from an external 240 V mains supply or optionally by the USB power bank charged by a PV panel. The power bank supplies continuous 5 V to the RPi and its peripherals, ensuring uninterrupted operation extending the system's autonomy in remote or off-grid locations. The 4G USB modem can added for data transmission, if remote access to the data or images are required.

2.3. Solar irradiance forecasting by the low-cost sky imager

2.3.1. Data collection

Once the KALiSI was fully operational, it was installed at the Karlsruhe Institute of Technology (KIT) Solar Park in Karlsruhe, Germany (49°05′56.2″N 8°26′14.5″E) on a 3 m-tall mast (see Fig. 2). To enable comparison of the forecasted SI values with experimental values, a calibrated SI sensor based on a temperature-corrected silicon (Si) cell (IMT Technology GmbH, Si-V-1.5TC-T, Germany) is mounted next to the

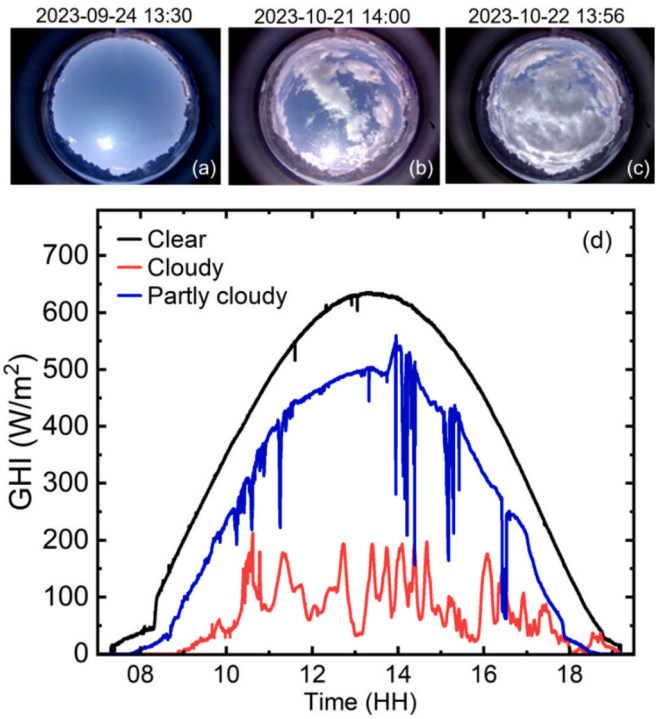

Fig. 3. Sample images with time stamps from the KALiSI under different sky conditions: (a) clear; (b) partly cloudy; (c) very cloudy or overcast. (d) The GHI measurements at 1 min resolution for a clear, partly cloudy, and cloudy days from the SI sensor are also plotted.

KALiSI for measurement of instantaneous GHI, with data logged directly on the KALiSI together with the images, also depicted in Fig. 2. Although such silicon SI sensors have a higher intrinsic uncertainty, particularly due to their limited spectral response in the shortwave region of the solar spectrum, the choice of this sensor used in the study has been motivated by four factors: i) its relatively low cost (e.g. the Si-based sensor used in this work costs less than one-third of the price of a typical thermopile pyranometer used in weather stations). Here it should also be noted that the cost of the SI sensor is already high compared to the remainder of the KALiSI system; ii) its ease of integration; iii) its direct relevance to photovoltaic applications; as well as iv) the authors' own experience with its proven robustness over the decades (e.g. see [55,56]). Overall, the use of a Si-based SI sensor is not expected to significantly impact the performance assessment.

KALiSI has been operational for over 1 year (since September 2023), where it has endured many days of rain, a few days of snow, and ambient temperatures ranging from −6 to + 35 °C. Its extensive outdoor operation demonstrates the optimal performance, robustness, and the imager's ability to withstand the weather of southwest Germany over prolonged periods.

Some of the captured sky images from the KALiSI for different daytime sky conditions are given in Fig. 3(a-c). It can be seen that the KALiSI is capable of accurately capturing the diverse atmospheric conditions. The clear sky image in Fig. 3(a) shows an instance of atmospheric visibility with no clouds within the hemispheric view of the camera. In contrast, the partially cloudy image (Fig. 3(b)) shows an example where clouds are scattered within the view, while the more overcast image (Fig. 3(c)) depicts clouds almost covering the entire sky view of the camera. The images show the ability of the KALiSI to capture a range of sky conditions, providing valuable data for analysis and SI forecasting. Fig. 3(d) shows some daily GHI profiles recorded under different weather conditions from the SI sensors for KALiSI. The clear day profile displays a smooth curve with high GHI levels, indicating minimal atmospheric interference. The partly cloudy profile shows some periods of

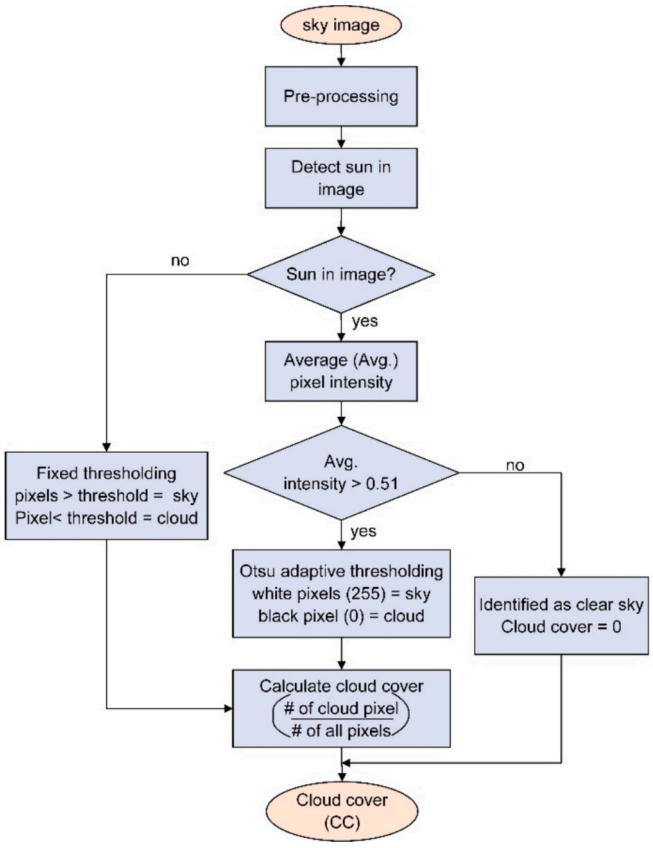

Fig. 4. Flow chart of cloud cover determination process employed in the KALiSI.

fluctuating GHI resulting from passing clouds, as evident by the dips in the profile, while the cloudy day profile exhibits consistently lower GHI levels, indicating reduced sunlight penetration during this day. Images from the KALiSI and corresponding GHI are collected and archived on an external hard storage drive in the enclosure.

As mentioned above and shown in Fig. 2, a commercial sky imager (EKO Instruments, CMS-Schreder, ASI-16, Austria, 5 MP, 180° field of view) is also installed on the same weather mast. The EKO all-sky imager (ASI) is installed with a dedicated horizontally mounted pyranometer (EKO Instruments, MS80HS, Japan) to automatically record the corresponding GHI with the captured JPEG images at 1-min intervals. The data are collected and archived on a server. The EKO ASI-16 sky camera includes external temperature and relative humidity sensors together with an integrated ventilation and heating system to enable it to withstand almost every weather condition. The heating system can prevent fogging, icing, and condensation on the lens, ensuring clear imagery, while the ventilation regulates internal temperature to prevent overheating. These not only protect the camera from environmental damage, extending its lifespan, but also enable continuous operation in extreme climates, ensuring accurate data collection and high-quality in almost any weather. The EKO AS1-16 was installed at the end of January 2024, several months after the low-cost system was deployed. Thus, for the purposes of comparison, data from 1 February to 31 July 2024 was collected from both cameras and selected for this work, with the exception of interruptions due to maintenance and technical challenges that resulted in about a total of 14 days of missing GHI or images or both from the two imagers. While larger datasets aid in better model generalisation and reduce overfitting, using 6 months of data for SI forecasting with DL models improves accuracy by capturing seasonal variations, diverse weather conditions, and diurnal cycles. This allows the model to learn the temporal dependencies well and results in more robust predictions. Due to weather conditions at the site (late winter to mid-summer), fully clear days are very limited during this period. Thus, it could be expected that the GHI, especially for clear days, might be harder to predict.

2.3.2. Data processing and cloud cover determination

The images captured by the KALSI are processed using OpenCV, an advanced image-processing library in Python. The images are firstly pre-processed by masking out the unwanted areas of each image as well as resizing them to make them suitable for cloud/sky segmentation and training the ML model. Images of poor quality, including those that are blurred or contain undesirable objects such as insects or birds (landing on the camera dome) and other unwanted objects were also removed manually by visual inspection. The sun's position in the image is detected using a thresholding method [57]. Specifically, the position is determined as the centroid of the largest area with pixel values in the red channel exceeding an empirically determined threshold of 240 pixels. This approach ensures that the detected sun position corresponds to the brightest region in the image, accounting for optical distortions and potential misalignments inherent in the imaging system. In cases where the sun is temporarily obscured by clouds, no such high-intensity region may be detected, and the sun's presence in the image is considered absent.

The cloud and sky pixels in the images are segmented following the hybrid thresholding procedure described by Li et al. [58] as follows.

- The images are separated into three categories: cloudy, partly cloudy, and clear. This classification is based on the average pixel intensity of the image area [59,60], excluding the region around the sun.
- A fixed threshold, determined empirically, is used to segment cloud pixels from sky pixels according to the pixel intensity in the image. This threshold is applied without additional processing when the sun is blocked (cloudy sky).
- When the sun is not blocked (clear or partly cloudy), the values of pixel intensity of the region around the sun are elevated due to the strong sunlight, especially on a clear day. Using a fixed threshold therefore may erroneously classify the sky area around the sun as a cloud [31,59].
- Consequently, for a partially cloudy sky, the image is binarised utilising the Otsu threshold method [38], whereas, for a clear sky, the cloud coverage is set to zero without further processing. The Otsu threshold method is robust and has flexibility in distinguishing between clouds and sky pixels. It involves the use of one-dimensional pixel intensity data hence its accuracy is not impacted by shape or geometric features.

The pixel segmentation is based on the R:B ratio image, which exhibits a higher contrast between the cloud and the sky in comparison to other techniques [61]. The cloud cover (cc) is subsequently computed from the segmented images using Eq. (1) [60]:

$$cc = N_{cloud}/N_{total} \tag{1}$$

where N_{cloud} and N_{total} are the number of cloud pixels, and total number of cloud and sky pixels in the image respectively. A flow chart of the main processing steps for cloud fraction determination is shown in Fig. 4.

Each image is associated with its corresponding cloud fraction and GHI measurement obtained from the SI sensor, which are logged directly on the KALiSI with the images. These measurements serve as the ground truth for predicting GHI from the images captured by the KALiSI system. Images without corresponding GHI measurements are discarded, likewise GHI measurements without corresponding images. The valid dataset from the low-cost imager consists of 125,883 sky images, which were collected between 1 February to 31 July 2024, along with corresponding GHI measurements and calculated cloud fraction. This data is

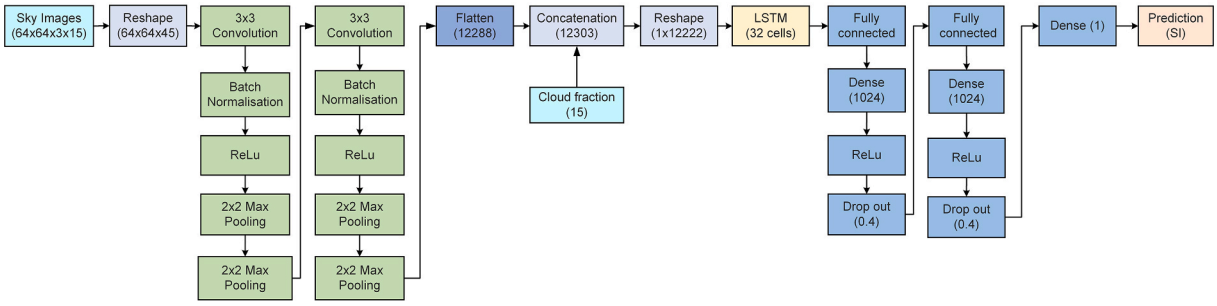

Fig. 5. Forecasting model structure used in KALiSI. The model takes sky images and cloud fraction data, calculated from the images, as input. The CNN processes the sky images to extract spatial features, while the cloud fraction is incorporated as an additional input to capture cloud coverage information. The extracted features and cloud data are concatenated and fed into the LSTM network, which handles temporal dependencies and patterns to predict future GHI.

split into the training and testing set. The test set is selected and set aside from the entire period of measurement, comprising 2838 observations from three consecutive days 23–25 June 2024. The three days were selected in order to capture the various patterns of sky conditions, thus, clear, partly cloudy and cloudy days, and are not used during the training phases. The remaining data is then allocated to the training and validation sets.

The pre-processed images were rescaled to 64 × 64 pixels and normalised in order to enable faster training time. The 64 × 64 resolution has been found to be appropriate for use in forecasting and maintains a reasonable training time and accuracy [38]. This resolution strikes a balance between computational efficiency and feature extraction capability, effectively preserving essential cloud patterns and significantly reducing computational complexity in deep learning applications for sky image analysis. Lower resolutions result in a noticeable loss of cloud details, negatively impacting model performance, whereas higher resolutions increase computational complexity without providing any substantial improvement in prediction accuracy. While this study focused on a 64 × 64 resolution due to these trade-offs, future work will explore higher resolutions. However, given the significantly increased computational and time demands, such an analysis is beyond the scope of this study.

The images are then stacked in sequences according to the forecast horizon, before being loaded as input to the CNN part of the model, in order to capture the dynamics of moving clouds. Furthermore, the collected GHI measurements are rescaled from W/m^2 to kW/m^2 to align with the normalised pixels of the images. The final dataset used after stacking in sequences of 15 (corresponding to a 15-min forecast horizon) consists of 113,260 and 2682 observations for training-validation and testing sets respectively.

The images collected from the ASI-16 commercial sky imager, along with the GHI measurements from its dedicated pyranometer (EKO Instruments, MS80HS, Japan), shown in Fig. 2, were also processed following the same protocol as described above for the KALiSI. The GHI from this pyranometer serves as the ground truth for forecasting GHI from ASI-16 images and for comparing the results with the KALiSI's forecast outputs. There is another pyranometer (Kipp & Zonen, SMP12, The Netherlands) shown in Fig. 2 that is not used in this work.

2.3.3. Forecasting model

A hybrid CNN-LSTM model is used with the CNN extracting local trends and features in the images while the LSTM captures and learns the dependencies and sequential relationships [62]. Such a combination can take full advantage of the strengths of each of the two models to improve the forecast ability of the final model. CNNs are known for having powerful feature-learning abilities and have been successfully employed in image processing [63]. The success of CNNs can be attributed to the stacking of multiple layers of convolutional operations, which enables the extraction of features from complex information, such as images. Although there are numerous CNN architectures available (including ResNet, AlexNet, VGG-16 and LeNet-5), they all follow the same basic concept. The input image is passed through several successive convolutional operations and then flattened to form a vector, which serves as a compact numerical representation of the learned features. This vector encapsulates essential image characteristics, which is fed into some fully connected layers to generate a regression result when predicting continuous data or a classification score when predicting categorical or discrete data [64].

Conversely, LSTM networks are well-suited to the handling of time-series data. They have demonstrated effective performance in SI forecasting for both short-term and long-term horizons [65]. Originally proposed by Hochreiter and Schmidhuber in 1997 [66], LSTM represents an enhanced form of recurrent neural network (RNN) that overcomes the limitations of traditional RNNs, including the problems of vanishing and explosion gradients [65]. An LSTM unit is composed of three gates (input, output and forget gates) with internal memory, which enables it to make a decision either to keep or forget the existing memory through the introduced gates [67]. This makes LSTM superior in dealing with sequential prediction tasks and successful in capturing long-term dependencies.

The structure of the proposed hybrid model, as shown in Fig. 5, follows the approach of El Alani et al. [32] and is based on the CNN architecture adapted from Sun et al. [43]. The CNN-LSTM forecasting model processes sky images using a CNN to extract high-level spatial features related to cloud structures. The CNN consists of two convolutional blocks, each composed of a convolutional layer, batch normalization, ReLU activation, and max-pooling. The use of two convolutional blocks ensures that both low-level edge features and higher-level cloud patterns are effectively captured before passing the data to the LSTM network. Batch normalization is applied after each convolution block to accelerate training and improve model stability. Once the CNN extracts spatial features, such as cloud texture, density, and distribution, the output is flattened into a one-dimensional vector, serving as a numerical representation of the essential image characteristics learned from the input images. This flattened vector is then concatenated with the cloud fraction, which provides additional physically meaningful information about sky conditions, complementing the CNN-extracted features. The combined feature vector is fed into an LSTM layer with 32 units, which captures temporal dependencies by analysing historical patterns in the data, enhancing the model's ability to forecast SI. The output from the LSTM network is then passed through fully connected layers with ReLU activation to introduce non-linearity, followed by Dropout layers to prevent overfitting. Finally, the model generates the SI predictions, taking advantage of both the spatial cloud features and temporal patterns learned from the data.

2.3.4. Model training

The network was implemented using the Keras TensorFlow deep learning package and trained using the stochastic gradient descent optimiser, Adam, a popular optimiser in the field of ML. The mean

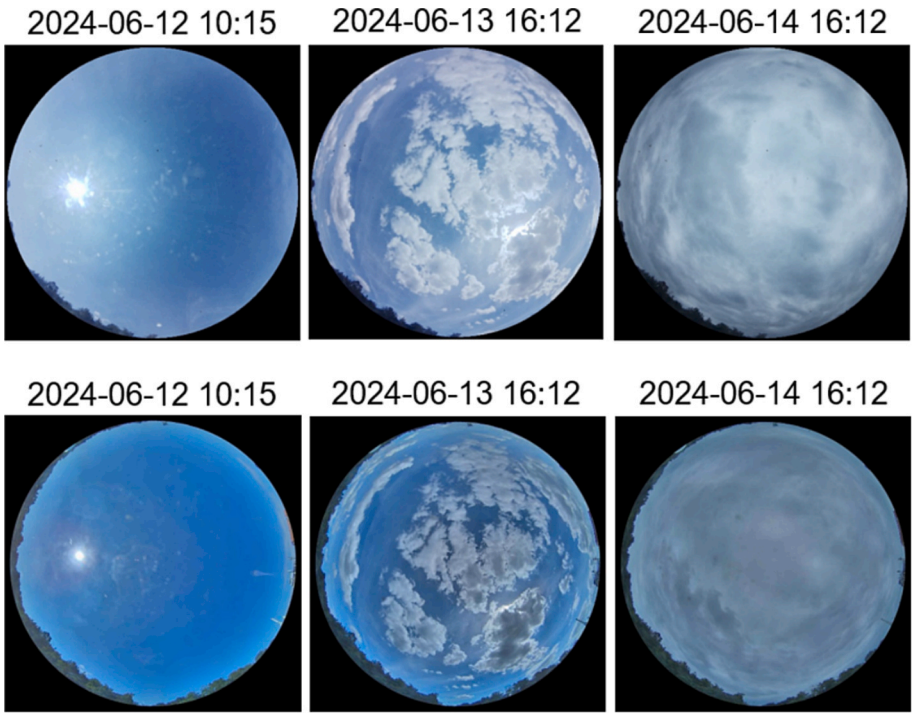

Fig. 6. Pre-processed images from the two imagers under different sky conditions with time stamps: (top row) KALiSI low-cost sky imager and (bottom row) EKO ASI-16 commercial sky imager.

squared (MS) error, in Eq. (2), is used as the loss function in the model. The loss function measures how far the predictions differ from the actual values in the data set. During the process of training, the model tries to minimise the loss function. The batch size and learning rate were varied to identify the optimal network architecture. As there is no fixed value in such ML models to explain the optimal design of models (due to the iterative training of networks within a model), the optimal parameters were determined using the errors during training and validation to assess the accuracy of the algorithms [36]. The 10-fold cross-validation technique was employed, whereby the training set is divided into 10 folds. Each of the 10 folds is used as the validation set in turn, while the other 9 folds are used together for training the model. This results in the training of 10 sub-models, with the final prediction taken as the ensemble mean of the sub-models.

$$MSerror = \frac{1}{N}\sum_{i=1}^{N}(y_{p,i} - y_{m,i})^2 \quad (2)$$

where $y_{p,i}$ and $y_{m,i}$ are the respective predicted and measured values, and N is the total number of data points.

2.3.5. Comparison of the low-cost imager and a commercial sky imager

A comparison of cloud fraction estimates from the KALiSI and ASI-16 was conducted using the same cloud algorithm described above to evaluate the agreement between these two independent imagers in terms of cloud fraction. Additionally, a comparison of forecasting performance using images from the ASI-16 and KALiSI was carried out to assess the model's performance when predicting SI with images from each sky imaging system. This analysis aimed to determine whether a €10,000 device provides any significant performance advantage over a system that is 20 times cheaper. Placing both cameras on the same mast ensured that they both have unobstructed view of the same sky dome information. The model was re-trained and tested using data from the EKO ASI-16.

Fig. 6 shows some images captured by the two cameras respectively at the same time. In order to focus on the essential difference between the low-cost sky imager and the commercial one, data pre-processing and algorithms used for the ASI-16 imager were made as consistent and similar to the KALiSI as possible. These side-by-side images provide a direct comparison of the visual output from the two imagers under identical sky conditions.

The images captured by the two different cameras under the same sky dome for different sky conditions shown in Fig. 6 exhibit subtle but important differences in lighting, exposure, and image quality. The top row images (KALiSI) appear brighter, with more pronounced sunlight glare, particularly on the clear sky instance (2024-06-12 10:15) indicating that the sensor may have higher light sensitivity or a greater exposure setting. In contrast, the bottom row (ASI-16) of the same clear sky instance shows less glare, producing a more evenly lit sky, which suggests the use of a filter or lower exposure setting to reduce brightness. Additionally, the KALiSI exhibits a slightly stretched appearance of clouds and horizon due to the high viewing angle (220°), while ASI-16 offers a more centred view (180°). Furthermore, the ASI-16 displays slightly more saturated colours, particularly in the blue tones, compared to the lighter hues in the KALiSI. These variations likely stem from differences in camera calibration, sensor quality, and lens characteristics, contributing to the subtle but distinct visual interpretations of the same sky conditions. The figure highlights the capability of the KALiSI to produce comparable images to those from a commercial imager, demonstrating its effectiveness in capturing varying sky conditions and potential for reliable sky imaging for SI forecasting at a reduced cost.

2.3.6. Performance evaluation

The performance of the prediction model from the low-cost system is evaluated using the RMS error and mean absolute (MA) error, defined in Eq. (3). and Eq. (4), respectively. The RMS error and MA error are some of the most widely used metrics for evaluating SI prediction accuracies. Smaller values of RMS error and MA error are an indication of lower deviation of the forecasted values from the measured and better predictive performance of the model. In order to make a meaningful comparison of the performance of the model when applied to data from the two different imaging systems, the RMS errors and MA errors are normalised to the mean of the measured data using Eq. (5) and Eq. (6) [68].

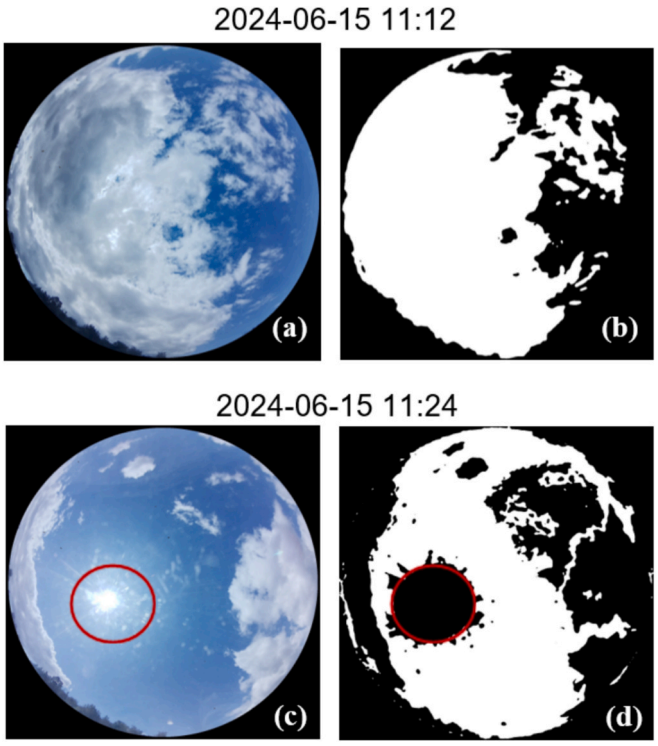

Fig. 7. Results of the cloud segmentation for cloud fraction calculation for two instances on 15 June 2024.

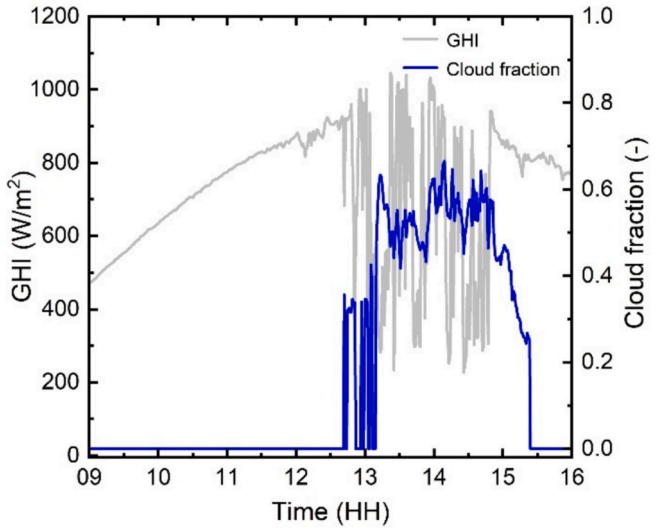

Fig. 8. Cloud fraction and corresponding GHI from the KALiSI of a typical mixed day captured on 10 June 2024 from 9:00 am to 4:00 pm.

This normalisation provides a more standardised way of measuring errors and enables a fair comparison across different models or datasets with varying scales [69].

$$\text{RMS error} = \sqrt{\frac{1}{N}\sum_{i=1}^{N}(\text{GHI}_{p,i} - \text{GHI}_{m,i})^2} \quad (3)$$

$$\text{MA error} = \frac{1}{N}\sum_{i=1}^{N}\left|(\text{GHI}_{p,i} - \text{GHI}_{m,i}\right| \quad (4)$$

$$\text{nRMS error} = \frac{\sqrt{N}}{\sum_{i}^{N}\text{GHI}_{m,i}}\sqrt{\frac{1}{N}\sum_{i=1}^{N}(\text{GHI}_{p,i} - \text{GHI}_{m,i})^2} \quad (5)$$

$$\text{nMA error} = \left(\frac{1}{\sum_{i}^{N}\text{GHI}_{m,i}}\right)\sum_{i=1}^{N}\left|(\text{GHI}_{p,i} - \text{GHI}_{m,i}\right| \quad (6)$$

where $GHI_{p,i}$ and $GHI_{m,i}$ are the respective predicted and measured GHI values in W/m^2, and N is the total number of times predictions are performed.

The persistence model, a commonly used reference model in SI forecasting, which always forecasts the last measured value irrespective of the time horizon is added as a reference model over the test set to also assess the performance of the model in forecasting. In SI forecasting, the persistence model assumes that the SI value at time $t + 1$, is the same as the SI value at time t as shown in Eq. (7) [70]:

$$\text{GHI}_{t+1} = \text{GHI}_{t} \quad (7)$$

3. Results and discussions

3.1. Low-cost sky imaging system

The KALiSI has been operational since September 2023, successfully capturing high-quality images with the exception of a few challenges encountered. Some of the challenges met during this period include the deposition of overnight dew on the protective dome, which can take time to dry out in the morning. Additionally, occasional condensation occurs within the dome in instances of sudden temperature fluctuations. Consequently, images are rendered blurry during these periods. To address these challenges, the integration of a defogger or heating element into the dome is planned for subsequent versions. This will facilitate the automatic drying of condensed water droplets, thereby ensuring clearer images. Furthermore, a cooling system is planned for integration into subsequent versions of the device to address the potential for elevated temperatures within the weatherproof enclosure in regions characterised by hot and humid climates. While these modifications will increase the overall cost of the system, the increase is expected to be very minimal due to the availability of inexpensive off-the-shelf electronic modules and sensors. These additions will protect the KALiSI, prolong its operational life and allow the camera to function reliably in harsh climates, ensuring consistent and quality data collection regardless of weather conditions.

3.2. Results of cloud fraction determination

The results of the cloud segmentation for cloud fraction calculation are shown in Fig. 7. Fig. 7(a) and (c) show the original pre-processed images, while Fig. 7(b) and (d) show the corresponding binary images respectively used in calculating cloud fraction. From Fig. 7(a) and (b) it can be seen that when the sun is obscured by thick clouds, there is a pronounced contrast between the cloud and sky pixels. In such cases, the fixed R:B ratio threshold method effectively discriminates between cloud and sky pixels. The white pixels represent the clouds, and the black pixels represent the sky. However, there were cases where the cloud pixels were almost indistinguishable from the sky pixels and were misclassified. When the clouds are particularly thin, the pixels are below the threshold and are not identified as clouds.

In the case of a partially cloudy sky, as given in Fig. 7(c) and (d), the Otsu thresholding method adapts the threshold to distinguish between cloud and sky pixels. Clouds are represented by the black pixels and the white pixels show the sky. Fig. 7(d) illustrates a situation where sky pixels close to the sun have been erroneously identified as cloud (black) pixels and are therefore considered as cloud when calculating the cloud fraction. It is necessary therefore to investigate other methods that can minimise the occurrence of some of these classification errors for the images from the KALSI. One option would be to crop out the sun and region around it before binarization. For clear sky conditions, the cloud fraction is set to zero without any processing.

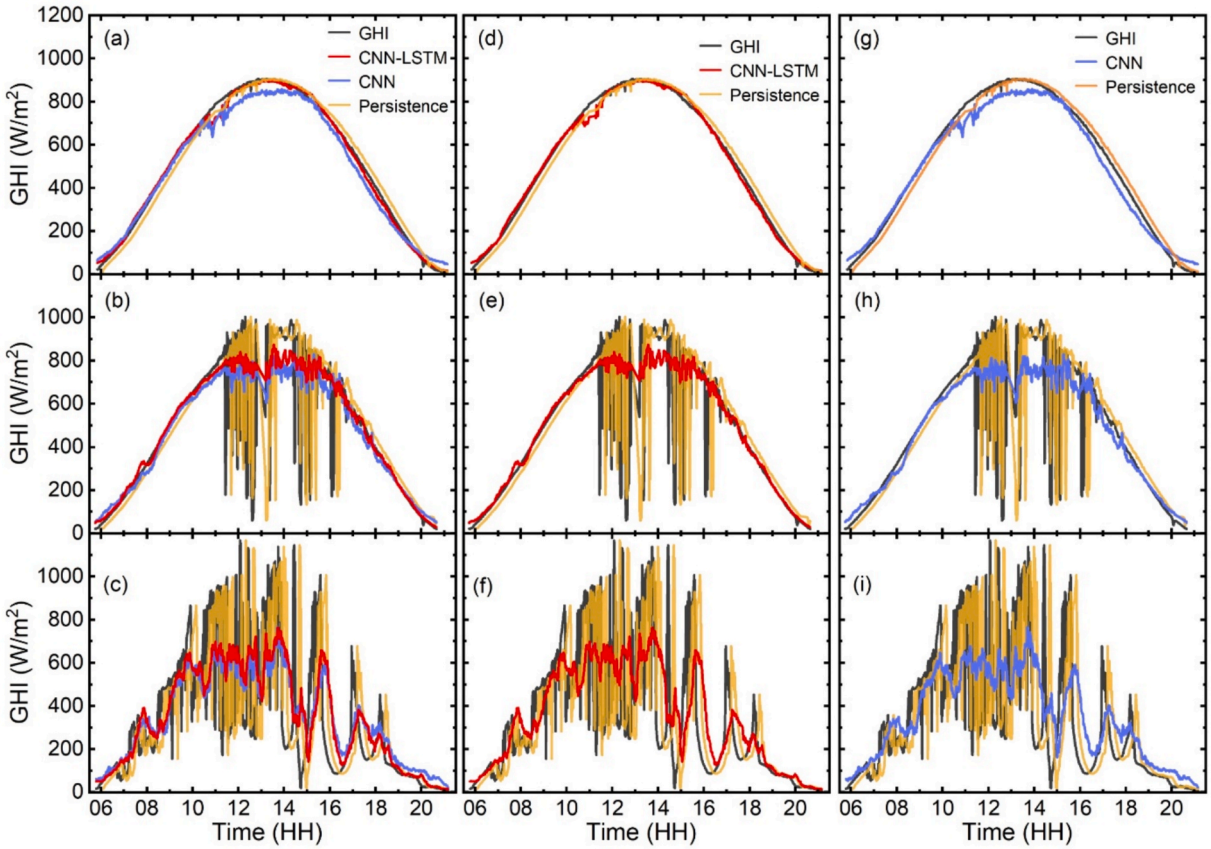

Fig. 9. Forecasting results of selected days from the KALiSI for CNN-LSTM, CNN and persistence models: The first column shows all three models for (a) clear day (25 June 2024), (b) partly cloudy day (24 June 2024), (c) cloudy day (23 June 2024). The second and third columns present the same days with the CNN-LSTM and CNN models, respectively, together with persistence.

Table 2
Performance for selected test days from the KALiSI in terms of RMS error and MA error. All values are in W/m^2.

	Clear		Partly cloudy		Cloudy		All	
	RMS error	MA error	RMS error	MA error	RMS error	MA error	RMS error	MA error
Persistence	33	30	192	98	256	159.2	161	96
CNN	44	36	145	83	**203**	149.1	130	89
CNN-LSTM	**20**	**15**	**141**	**67**	206	**144**	**122**	**75**

The calculated cloud fractions for a specified period in a day of mixed-sky conditions are shown in Fig. 8, along with the corresponding GHI measurements. As can be observed, the day is predominantly characterised by clear sky conditions in the morning, with the advent of cloud cover occurring shortly after midday. During the period of clear sky conditions, the cloud fractions are set to zero, in accordance with the cloud fraction algorithm. Furthermore, the GHI demonstrates a gradual increase throughout this period until after midday, when transient clouds are observed. As the clouds passed the sky, the cloud fraction increased while the GHI declined until the sky became clear after all the clouds had passed. The cloud fraction subsequently reaches zero, accompanied by a corresponding increase in the GHI.

3.3. Forecasting results

The performance of the hybrid CNN-LSTM model with images from KALiSI is evaluated under three different weather scenarios: clear, partially cloudy and cloudy conditions. A full day of each weather condition was analysed. The results were assessed by comparing with CNN model and persistence (as reference) models over the days selected. The CNN model is taken as the CNN part of the hybrid model without any modifications. This was done to assess whether or not combining the CNN with LSTM improves the GHI forecasting task. The results obtained for 15-min ahead GHI forecasting for each weather scenario is presented in Fig. 9 and shown in detail in Table 2.

It is observed that the CNN-LSTM model outperforms the persistence (reference) model as well as the CNN model under all weather conditions. Indeed, the model achieves an overall RMS error of 122 W/m^2 MA error of 75 W/m^2 and the the persistence achieves overal RMS error and MA error of 161 W/m^2 and 96 W/m^2 respectively. However, the model shows the best performance under clear sky conditions when forecasting SI with images from the KALiSI. On the selected clear day, the model predicts GHI with RMS error of 20 W/m^2 and MA error of 15 W/m^2. On the partly cloudy day, the CNN–LSTM model also exhibits better performance compared to CNN and persistence, despite a rather high RMS error and MA error values. The RMS error of the model on this day is 141 W/m^2 and the MA error is 67 W/m^2. while the RMS errors of the persistence and CNN are 145 and 192 W/m^2, and MA errors are 83 and 97 W/m^2, respectively. Unsurprisingly, the highest errors are observed on the cloudy day. While the forecasting uncertainties are particularly high for the cloudy day, the CNN–LSTM model still outperforms the persistence model for the 15 min. ahead forecast in terms of RMS error

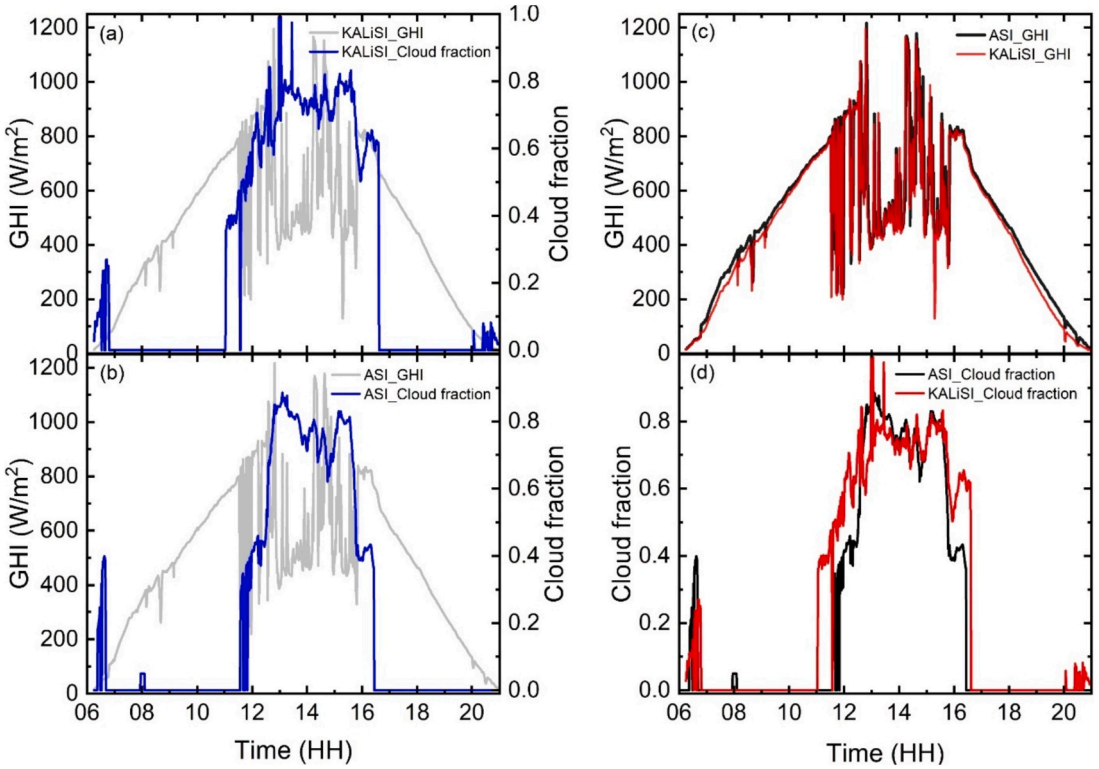

Fig. 10. Comparison cloud fraction estimate made by the KALiSI and ASI. (a) cloud fraction from KALiSI with corresponding GHI; (b) cloud fraction from ASI with corresponding GHI; (c) compares the GHI measurements from both systems and (d) compares the cloud fractions from both systems.

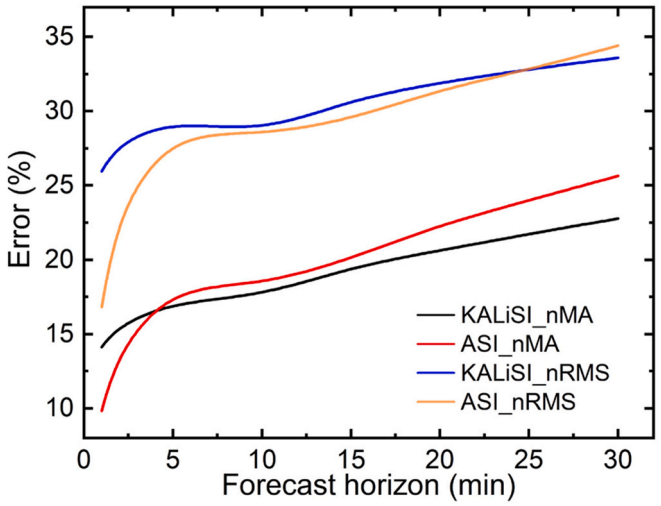

Fig. 11. Overall normalised errors (%) of the CNN-LSTM forecast performance for the two imagers over varying forecast horizons for the selected testing days.

and MA error. The RMS error of the CNN-LSTM model is slightly above that of the CNN model; however, the MA error is well below that of the CNN. The RMS and MA errors of the CNN–LSTM model under this weather condition is less than that of the persistence model as seen in Table 2, indicating a better reliability of the CNN-LSTM model than persistence under this challenging condition. These results demonstrate that the CNN–LSTM model is effective in forecasting GHI across the different weather conditions thus clear, partly cloudy and cloudy, particularly excelling over the persistence model on clear days. The results further show that using only images and cloud fraction (calculated from the images) in forecasting SI can provide competitive forecast performance in comparison to the work of El Alani et al. [32] which considers historical GHI data, and meteorological data in addition to the sky images. This is advantageous because the elimination of historical GHI data and/or other meteorological data reduces the computational complexity of the model, and makes it more applicable in areas where these data may be difficult to obtain or completely not available.

3.4. Comparison results

3.4.1. Cloud fraction comparison

The cloud fraction of another typical mixed day (17 July 2024) from

Table 3
Normalised RMS (%) error of CNN-LSTM forecast from two imagers.

Horizon	Sunny		Partly cloudy		Cloudy		All	
	KALiSI	ASI	KALiSI	ASI	KALiSI	ASI	KALiSI	ASI
1-min	3.4	6.8	28.1	18.1	46.4	25.5	27.9	16.8
2-min	3.4	7.3	29.6	24.4	50.6	38.7	27.9	23.5
5-min	3.5	7.3	29.7	28.4	54.8	50.1	29.4	28.6
10-min	3.5	4.9	28.8	28.6	53.3	51.7	28.5	28.4
15-min	3.8	5.1	28.1	27.7	60.5	55.5	30.8	29.4
20-min	3.8	7.0	28.9	28.0	63.2	59.3	31.9	31.5
25-min	3.5	7.8	29.6	28.2	65.3	62.4	32.8	32.8
30-min	5.2	9.3	29.9	28.6	65.7	65.4	33.6	34.4

Table 4
Normalised MA error (%) of CNN-LSTM forecast from the two imagers.

Horizon	Sunny		Partly cloudy		Cloudy		All	
	KALiSI	ASI	KALiSI	ASI	KALiSI	ASI	KALiSI	ASI
1-min	2.5	5.6	11.8	9.8	28.2	14.0	14.1	9.8
2-min	2.6	6.1	12.8	12.7	31.4	23.3	15.6	14.0
5-min	2.7	6.1	13.2	15.8	35.6	32.6	17.2	18.2
10-min	2.6	4.0	12.5	15.6	37.4	35.3	17.3	18.3
15-min	3.0	4.2	13.4	15.7	42.2	40.3	19.5	20.1
20-min	3.0	6.0	13.7	16.8	45.1	44.3	20.6	22.4
25-min	2.9	6.5	14.5	17.4	47.8	48.0	21.7	24.0
30-min	4.5	7.8	14.8	18.1	49.0	51.0	22.8	25.7

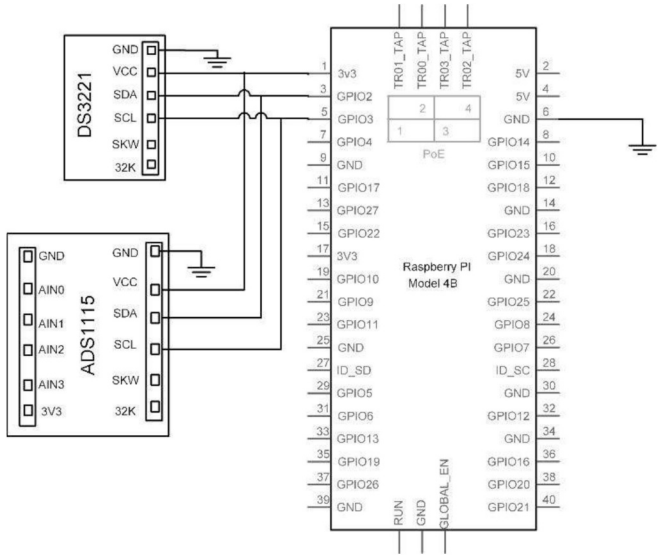

Fig. A1. Electronic schematic of the KALiSI showing the connection of the RTC and the ADC to RPI.

the KALiSI and ASI systems is shown in Fig. 10, along with the corresponding GHI measurements from both cameras. These data represent all available coincidences of the processed dataset, thus those remaining after preprocessing and validation, covering the period from sunrise to sunset. The objective here is to evaluate the agreements or otherwise in cloud fraction estimates produced by the same algorithm when applied to images from the two different. Fig. 10(a) presents the cloud fraction derived from the KALiSI, alongside the corresponding GHI measured by the SI sensor, while Fig. 10(b) shows the cloud fraction from ASI with its corresponding GHI measured by the pyranometer. Fig. 10(c) and (d) compare the GHI and cloud fraction from both systems, respectively. The GHI measurements from the SI sensor (used in KALiSI) and the pyranometer (used in ASI) follow similar trends, with minor differences that can be attributed to potential sensor sensitivity variations or differences in response time. Likewise, the cloud fraction estimates from both imaging systems correlate well with the GHI measurements and remain largely consistent with each other. However, there is a general tendency for the KALiSI to produce slightly higher cloud fraction estimates compared to the ASI. This discrepancy is likely due to the different image sensor and lens characteristics, which necessitate slightly different thresholding parameters in the image processing and cloud fraction determination algorithm.

3.4.2. Forecast comparison

The CNN-LSTM forecast results using images from the two cameras (KALiSI and EKO ASI-16) are compared according to the nRMS errors and nMA errors on the test testing set over a range of forecast horizons. This was done to explore the applicability of the proposed model to forecasting different time horizons, as well as to compare the performance of the model on images from a different sky imager. The aim was also to assess the suitability of the low-cost imagers for forecasting applications. In particular, experiments are conducted with future predictions for 1, 2, 5, 10, 20, 25 and 30 mins. intervals, following the same approach used for the 15-min predictions. The forecast results of the model for the two imagers over for the different horizons are shown in Figs. A3 and A4 respectively in the Appendix. Experiments with forecast horizons exceeding 30 min were not included in the analysis, as the resulting accuracy was deemed to be significantly the same as the 30 min horizon and did not demonstrate any discernible improvement in forecast performance. The results are presented in Tables 3 and 4, as well as in Fig. 11. Fig. 11 illustrates the evolution of the overall nRMS errors and nMA errors for the two imagers over varying forecast horizons. The overall nRMS error and nMA error are calculated as the averages of the errors for the different forecast horizons, respectively.

The overall nRMS errors, illustrated in Fig. 11(gold and blue lines), tend to increase with the forecast horizon for each camera, with an initial rapid increase up to the 5 mins mark. After this initial rise, the error trends somewhat stabilize and both lines show a gradual increase up until the 30 min forecast horizon. The ASI (gold line) shows a notable, consistently lower nRMS error values than the KALiSI (blue line), but slightly higher after the 25 min horizon. These suggest that the ASI enables more accurate forecasts than the KALiSI as revealed in Table 3 especially on cloudy and partly cloudy days. The behaviour of the nMA errors, also shown in Fig. 11(red and black lines), as well as in Table 4, is similar to the nRMS errors. The overall nMA error from the ASI (red line) is better than the KALiSI (black line). The nMA error of the KALiSI is lower (better performance) than the ASI up to the 5 min horizon mark, increases more rapidly and becomes higher than ASI afterward and continues steadily. The gap between the lines remains almost consistent after 5 min horizon and slightly widens out toward the 20 min horizon. The ASI generally exhibits a better performance in terms of the overall nMA errors in comparison to the KALiSI system, although the latter exhibits better performance on clear days as evidenced in Table 4.

Although there is generally a slight decrease in the model's overall performance when images from the low-cost camera are used, in comparison to the commercial system, the KALiSI can be a viable alternative for installation in PV-powered systems, especially in small-scale systems and weather stations for SI forecasting and other similar applications, due to its low cost, easy maintenance, and replacement of components. The simplicity and robustness of the system, coupled with its forecasting capabilities, render it an attractive alternative. This work demonstrates that DL models for SI forecasting based exclusively on sky images can provide competitive performance for very short-term SI forecasts. An increase in the size of the data set and including additional features like meteorological and GHI data could result in forecasts as accurate as those reported in the literature. However, the focus of this study is to avoid the use of meteorological and historical data as additional input to the model. Given the low equipment cost and affordability, the sky camera could be a potential alternative to traditional meteorological devices for on-site weather monitoring. It is important to note, however, that certain limitations must be addressed in order to ensure the

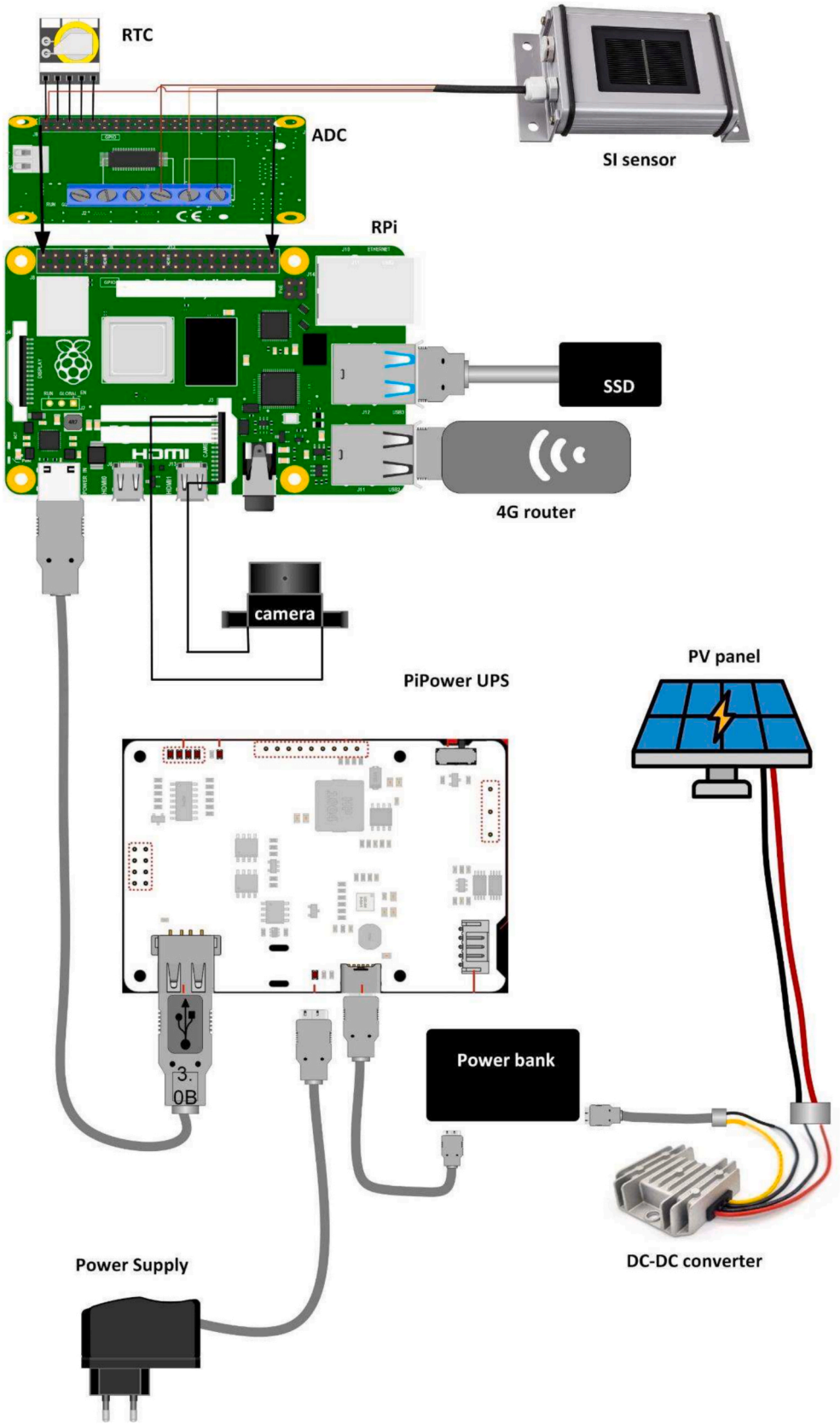

Fig. A2. Pictorial schematic showing the connection of the various components to the RPi including the optional components.

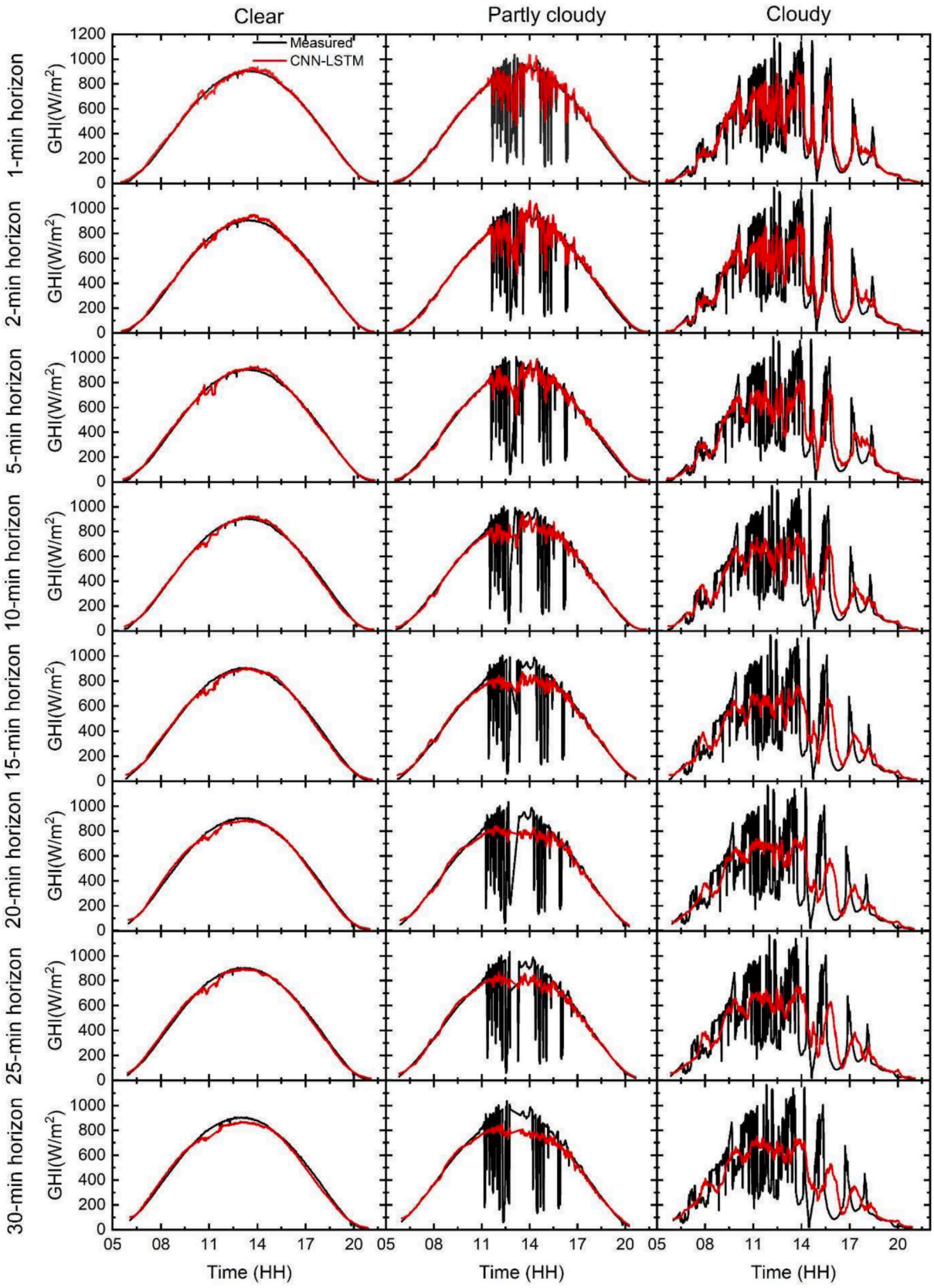

Fig. A3. Results for different forecast horizons (2, 5, 10, and 15 and 20 mins) from KALiSI for comparison of measured GHI (black) and CNNL-STM model predictions (red) under varying weather conditions: Clear (2024-06-25), Partly Cloudy (2024-06-24), and Cloudy (2024-06-23). Each row represents a different forecast horizon, while the columns depict different weather scenarios.

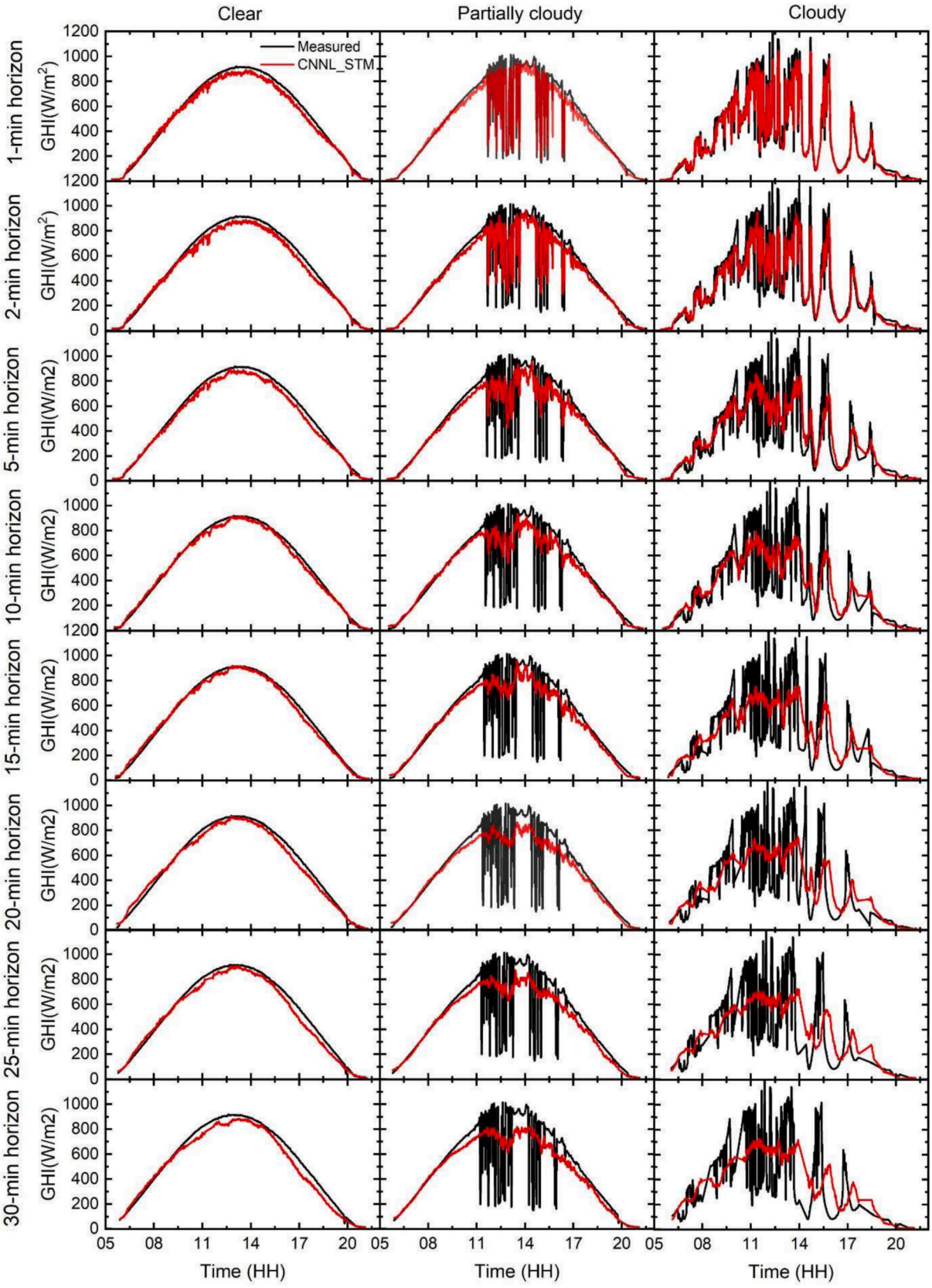

Fig. A4. Results for different forecast horizons (2, 5, 10, 15 and 20) from EKO ASI-16 for comparison of measured GHI (black) and CNNL-STM model predictions (red) under varying weather conditions: Clear (2024-06-25), Partly Cloudy (2024-06-24), and Cloudy (2024-06-23). Each row represents a different forecast horizon, while the columns depict different weather scenarios.

Table A1
The cost of main components used in KALiSI.

Component	Cost (€)
Raspberry Pi 4 Model-B 8 GB RAM	90.00
Raspberry Pi 8 MP Camera v2.1	20.00
Raspberry Pi power supply	15.00
Entaniya Fisheye 220° lens	25.00
Entaniya weatherproof dome	40.00
Real-time clock module	5.00
ADC module	20.00
256 GB SSD external storage	150.00
32 GB microSDXC memory card	15.00
SunFounder UPS	40.00
Weatherproof ABS plastic box	25.00
Miscellaneous consumables(jumper cables, silicone adhesive, screws, cable glands, etc)	100.00
Total Cost – basic version	**520.00**
– Optional items –	
50 W PV panel	55.00
30000 mAh power bank	39.00
50 W DC-DC converter	20.00
4G modem	35.00
Solar irradiance sensor	230.00
Total Cost – advanced version	**899.00**

successful future deployment of the camera for forecasting purposes. The dataset included images with notable disturbances, such as objects, birds and insects obstructing the sensor, as well as camera malfunctions that resulted in the loss of a few weeks of data. Missing data and low-quality images can introduce significant biases. The data used here spanned six months; however, DL models require a substantial amount of data for optimal performance. For sky image-based SI forecasting, it is recommended to train and validate models using at least two years of data and to test them with an additional year of data [71].

4. Conclusion

A low-cost all-sky imaging system (KALiSI) based on the RPi single-board computer and open-source software packages for SI prediction has been developed. Extensive testing and outdoor operation, as well as the quality of the images captured, demonstrate the optimal performance of the camera and its ability to withstand the weather of southwest Germany over long periods of time. However, future versions of this low-cost system will include additional cooling and/or heating systems to address the issues of overnight due settling and staying on the dome for longer periods and occasional moisture condensation inside the plastic dome in areas with extremely low temperatures or very hot and humid climates (with prolonged elevated temperatures). The availability of inexpensive off-the-shelf electronic modules and sensors will allow for the integration into the current design at relatively low cost, along with temperature and humidity monitoring sensors for controlling the heating/cooling system. There is also the need for long term deployment and monitoring to understand life span of the system and how environmental wear and tear affect the life span.

Images captured by the low-cost imaging system have been utilised in SI forecasting with a hybrid DL approach which combines CNN with LSTM techniques. The hybrid model was used to perform forecasting for GHI, 15 min ahead of time. Two evaluation metrics, RMS error and MA error, were used to assess the performance of the model. The CNN-LSTM-based approach achieved RMS error between 19 and 206 W/m^2 and MA error ranging from 15 to 144 W/m^2 depending on the sky conditions. The cloud cover determined as well as the forecasting performance from the low-cost sky imaging system has also been compared to that of a commercial, EKO-ASI-16 system. The protocol involved a similar cloud fraction calculation algorithm and forecasting model adapted to this imager. The comparison of the forecast performance was based on nRMS errors and nMA errors over varying forecast horizons. The cloud fraction from the low-cost system correlated well with the GHI measurements and was consistent with that from the commercial sky imager. However, the AS-16 showed better results than the low-cost system in terms of overall nRMS error and nMA error for every time horizon. This suggests that the low-cost camera developed is suitable for applications in short-term SI forecasting and could have great potential in SI forecasting in PV-powered systems, especially in developing countries in Africa. There is however the need to refine the image processing algorithms for better cloud detection and classification as well as incorporating weather sensors, such as temperature and humidity sensors, which could also improve forecasting accuracy by providing more detailed atmospheric data.

Future work will entail adapting and optimising the model for different imagers and forecast horizons and retraining with a larger dataset as well as the deployment of the forecasting model on a RPi as solar irradaince forecasting system (SIFS) for on-line prediction in PV-powered systems, especially small-scale systems. This will require a modification of the Python program scripts for capturing and saving images to include online image processing and cloud fraction determination and subsequent inclusion of the offline trained model. The SIFS will also include a signal conversion subsystem that will convert the forecast information into a suitable signal that can be used in control systems. Furthermore, multiple units of this imaging system are planned for deployment in Africa, where it is expected to have great potential and added value, to evaluate its operation in different climates and seasons. The current version of the imaging system will be upgraded with cooling and heating systems to ensure successful operation in different climates. Data from these systems will be used in a multi-site SI forecast to predict PV power generation across the areas of installation.

CRediT authorship contribution statement

Martin Ansong: Writing – original draft, Visualization, Validation, Software, Methodology, Investigation, Formal analysis, Data curation, Conceptualization. **Gan Huang:** Writing – review & editing, Resources, Methodology. **Thomas N. Nyang'onda:** Writing – review & editing, Supervision, Resources, Project administration, Funding acquisition. **Robinson J. Musembi:** Writing – review & editing, Supervision, Project administration, Funding acquisition. **Bryce S. Richards:** Writing – review & editing, Visualization, Supervision, Resources, Project administration, Methodology, Funding acquisition, Conceptualization.

Declaration of Competing Interest

The authors declare that they have no known competing financial interests or personal relationships that could have appeared to influence the work reported in this paper.

Acknowledgements

The authors acknowledge the Ph.D. scholarships for MA from the German Academic Exchange Services (DAAD) and the PASET Regional Scholarships and Innovation Fund (RSIF); the financial support provided by the Helmholtz Association via (i) the Recruitment Initiative Funding to BSR and (ii) the Research Field Energy Program-Materials and Technologies for the Energy Transition-Topic 1 Photovoltaics (38.01.05).

Appendix

Appendix A. Supplementary data

Supplementary data to this article can be found online at https://doi.org/10.1016/j.solener.2025.113516.

Data availability

Data and models are available from the authors per reasonable request. Additionally, models, scripts and a full list of parts used in the development of the low-cost camera system can be accessed on the GitHub repository at https://github.com/KALiSI4SIFS/KALiSI.git.

References

[1] International Energy Agency (IEA), Renewable 2023. 2024: Paris p. 141.
[2] M. Suri, T. Huld, T. Cebecauer, E.D. Dunlop, Geographic aspects of photovoltaics in Europe: Contribution of the PVGIS website, IEEE J. Sel. Top. Appl. Earth Obs. Remote Sens. 1 (1) (2008) 34–41.
[3] REN21, Renewables 2014 global status report. 2014: Paris, France.
[4] G. Masson, M.d. l'Epine, I. Kaizuka, International Energy Agency-Photovoltaic Power Systems Programme (IEA-PVPS) Trends in Photovoltaic Applications 2023.
[5] H. Zhou, Y. Zhang, L. Yang, Q. Liu, K. Yan, Y. Du, Short-term photovoltaic power forecasting based on long short term memory neural network and attention mechanism, IEEE Access 7 (2019) 78063–78074.
[6] M. Krechowicz, A. Krechowicz, L. Lichołai, A. Pawelec, J.Z. Piotrowski, A. Stępień, Reduction of the risk of inaccurate prediction of electricity generation from PV farms using machine learning, Energies 15 (11) (2022) 4006.
[7] D. Nikodinoska, M. Käso, F. Müsgens, Solar and wind power generation forecasts using elastic net in time-varying forecast combinations, Appl. Energy 306 (2022) 117983.
[8] M.Q. Raza, M. Nadarajah, C. Ekanayake, On recent advances in PV output power forecast, Sol. Energy 136 (2016) 125–144.
[9] S. Sobri, S. Koohi-Kamali, N.A. Rahim, Solar photovoltaic generation forecasting methods: A review, Energ. Conver. Manage. 156 (2018) 459–497.
[10] L. Vallance, B. Charbonnier, N. Paul, S. Dubost, P. Blanc, Towards a standardized procedure to assess solar forecast accuracy: A new ramp and time alignment metric, Sol. Energy 150 (2017) 408–422.
[11] K. Barhmi, C. Heynen, S. Golroodbari, W. van Sark, A review of solar forecasting techniques and the role of artificial intelligence, Solar 4 (1) (2024) 99–135.
[12] C. Brunet, O. Savadogo, P. Baptiste, M.A. Bouchard, Shedding some light on photovoltaic solar energy in Africa – A literature review, Renew. Sustain. Energy Rev. 96 (2018) 325–342.
[13] M. Ansong, T.N. Nyang'onda, R.J. Musembi, B.S. Richards. IEEE PES, IAS PowerAfrica. Very Short-Term Solar Irradiance Forecasting for Photovoltaic Power Integration with the Grid: Potentials and Challenges for Africa. in 2024 IEEE PES/IAS PowerAfrica. 2024.
[14] C.W. Chow, B. Urquhart, M. Lave, A. Dominguez, J. Kleissl, J. Shields, B. Washom, Intra-hour forecasting with a total sky imager at the UC San Diego solar energy testbed, Sol. Energy 85 (11) (2011) 2881–2893.
[15] H. Yang, B. Kurtz, D. Nguyen, B. Urquhart, C.W. Chow, M. Ghonima, J. Kleissl, Solar irradiance forecasting using a ground-based sky imager developed at UC San Diego, Sol. Energy 103 (2014) 502–524.
[16] C.-L. Fu, H.-Y. Cheng, Predicting solar irradiance with all-sky image features via regression, Sol. Energy 97 (2013) 537–550.
[17] R. Marquez, C.F.M. Coimbra, Intra-hour DNI forecasting based on cloud tracking image analysis, Sol. Energy 91 (2013) 327–336.
[18] B. Urquhart, M. Ghonima, D. Nguyen, B. Kurtz, C.W. Chow, J. Kleissl, Sky-Imaging Systems for Short-Term Forecasting, in: J. Kleissl (Ed.), Solar Energy Forecasting and Resource Assessment, Academic Press, Boston, 2013, pp. 195–232.
[19] R. Samu, M. Calais, G.M. Shafiullah, M. Moghbel, M.A. Shoeb, B. Nouri, N. Blum, Applications for solar irradiance nowcasting in the control of microgrids: A review, Renew. Sustain. Energy Rev. 147 (2021) 111187.
[20] C.F.M. Coimbra, J. Kleissl, R. Marquez, Chapter 8 - Overview of solar-forecasting methods and a metric for accuracy evaluation, in: J. Kleissl (Ed.), Solar Energy Forecasting and Resource Assessment, Academic Press, Boston, 2013, pp. 171–194.
[21] R.H. Inman, H.T.C. Pedro, C.F.M. Coimbra, Solar forecasting methods for renewable energy integration, Prog. Energy Combust. Sci. 39 (6) (2013) 535–576.
[22] B. Yang, T. Zhu, P. Cao, Z. Guo, C. Zeng, D. Li, Y. Chen, H. Ye, R. Shao, H. Shu, T. Yu, Classification and summarization of solar irradiance and power forecasting methods: A thorough review, CSEE J. Power Energy Syst (2021) 1–19.
[23] T. Jamal, G.M. Shafiullah, C. Carter, S.M. Ferdous, M. Rahman, Benefits of Short-term PV Forecasting in a Remote Area Standalone Off-grid Power Supply System. in 2018 IEEE Power & Energy Society General Meeting (PESGM). 2018.
[24] E.B. Ssekulima, M.B. Anwar, A. Al Hinai, M.S. El Moursi, Wind speed and solar irradiance forecasting techniques for enhanced renewable energy integration with the grid: a review, IET Renew. Power Gener. 10 (7) (2016) 885–989.
[25] D.W. Slater, C.N. Long, T.P. Tooman, Total Sky Imager/Whole Sky Imager Cloud Fraction Comparison. in Eleventh ARM Science Team Meeting 2001. Atlanta, Georgia.
[26] J.E. Shields, M.E. Karr, R.W. Johnson, A.R. Burden, Day/night whole sky imagers for 24-h cloud and sky assessment: history and overview, Appl. Opt. 52 (8) (2013) 1605–1616.
[27] J. Yang, Q. Min, W. Lu, W. Yao, Y. Ma, J. Du, T. Lu, G. Liu, An automated cloud detection method based on the green channel of total-sky visible images, Atmos. Meas. Tech., 8 (11) (2015) 4671–4679.
[28] A. Heinle, A. Macke, A. Srivastav, Automatic cloud classification of whole sky images, Atmos. Meas. Tech., 3 (3) (2010) 557–567.
[29] S. Quesada-Ruiz, Y. Chu, J. Tovar-Pescador, H.T.C. Pedro, C.F.M. Coimbra, Cloud-tracking methodology for intra-hour DNI forecasting, Sol. Energy 102 (2014) 267–275.
[30] A. Al-lahham, O. Theeb, K. Elalem, T.A. Alshawi, S.A. Alshebeili, Sky imager-based forecast of solar irradiance using machine learning, Electronics 9 (10) (2020) 1700.
[31] M. Caldas, R. Alonso-Suárez, Very short-term solar irradiance forecast using all-sky imaging and real-time irradiance measurements, Renew. Energy 143 (2019) 1643–1658.
[32] O. El Alani, M. Abraim, H. Ghennioui, A. Ghennioui, I. Ikenbi, F.-E. Dahr, Short term solar irradiance forecasting using sky images based on a hybrid CNN–MLP model, Energy Rep. 7 (2021) 888–900.
[33] S.R. West, D. Rowe, S. Sayeef, A. Berry, Short-term irradiance forecasting using skycams: Motivation and development, Sol. Energy 110 (2014) 188–207.
[34] H.-M. Zuo, J. Qiu, Y.-H. Jia, Q. Wang, F.-F. Li, Ten-minute prediction of solar irradiance based on cloud detection and a long short-term memory (LSTM) model, Energy Rep. 8 (2022) 5146–5157.
[35] S. Tiwari, R. Sabzehgar, M. Rasouli, Short Term Solar Irradiance Forecast based on Image Processing and Cloud Motion Detection. in 2019 IEEE Texas Power and Energy Conference (TPEC), 2019.
[36] R.A. Rajagukguk, R. Kamil, H.-J. Lee, A deep learning model to forecast solar irradiance using a sky camera, Appl. Sci. 11 (11) (2021) 5049.
[37] Y. Nie, X. Li, A. Scott, Y. Sun, V. Venugopal, A. Brandt, SKIPP'D: A SKy images and photovoltaic power generation dataset for short-term solar forecasting, Sol. Energy 255 (2023) 171–179.
[38] Y. Sun, G. Szűcs, A.R. Brandt, Solar PV output prediction from video streams using convolutional neural networks, Energ. Environ. Sci. 11 (7) (2018) 1811–1818.
[39] J. Zhang, R. Verschae, S. Nobuhara, J.-F. Lalonde, Deep photovoltaic nowcasting, Sol. Energy 176 (2018) 267–276.
[40] N.Y. Hendrikx, K. Barhmi, L.R. Visser, T.A. de Bruin, M. Pó, A.A. Salah, W.G.J.H. M. van Sark, All sky imaging-based short-term solar irradiance forecasting with Long Short-Term Memory networks, Sol. Energy 272 (2024) 112463.
[41] Q. Paletta, G. Arbod, J. Lasenby, Benchmarking of deep learning irradiance forecasting models from sky images – An in-depth analysis, Sol. Energy 224 (2021) 855–867.
[42] D. Pothineni, M.R. Oswald, J. Poland, M. Pollefeys, KloudNet: Deep Learning for Sky Image Analysis and Irradiance Forecasting, Springer International Publishing, Cham, 2019.
[43] Y. Sun, V. Venugopal, A.R. Brandt, Short-term solar power forecast with deep learning: Exploring optimal input and output configuration, Sol. Energy 188 (2019) 730–741.
[44] C. Feng, J. Zhang, SolarNet: A sky image-based deep convolutional neural network for intra-hour solar forecasting, Sol. Energy 204 (2020) 71–78.
[45] B. Urquhart, B. Kurtz, E. Dahlin, M. Ghonima, J.E. Shields, J. Kleissl, Development of a sky imaging system for short-term solar power forecasting, Atmos. Meas. Tech., 8 (2) (2015) 875–890.
[46] P. Shaffery, A. Habte, M. Netto, A. Andreas, V. Krishnan, Automated construction of clear-sky dictionary from all-sky imager data, Sol. Energy 212 (2020) 73–83.
[47] C. Feng, D. Yang, B.-M. Hodge, J. Zhang, OpenSolar: Promoting the openness and accessibility of diverse public solar datasets, Sol. Energy 188 (2019) 1369–1379.
[48] S. Dev, F. Savoy, Y.H. Lee, S. Winkler, WAHRSIS: A low-cost high-resolution whole sky imager with near-infrared capabilities. SPIE Defense + Security. Vol. 9071. 2014: SPIE.
[49] A. Kazantzidis, P. Tzoumanikas, A.F. Bais, S. Fotopoulos, G. Economou, Cloud detection and classification with the use of whole-sky ground-based images, Atmos. Res. 113 (2012) 80–88.
[50] W. Richardson, H. Krishnaswami, R. Vega, M. Cervantes, A low cost, edge computing, all-sky imager for cloud tracking and intra-hour irradiance forecasting, Sustainability 9 (4) (2017) 482.
[51] M. Jain, V.S. Sengar, I. Gollini, M. Bertolotto, G. McArdle, S. Dev, 2022 LAMSkyCam: A low-cost and miniature ground-based sky camera. HardwareX, 2022, p. 12.
[52] T. Schmidt, J. Stührenberg, N. Blum, J. Lezaca, A. Hammer, T. Vogt, A network of all sky imagers (ASI) enabling accurate and high-resolution very short-term forecasts of solar irradiance. in 21st Wind & Solar Integration Workshop (WIW 2022), 2022.
[53] Y. Traonmilin, C. Aguerrebere, Simultaneous high dynamic range and superresolution imaging without regularization, SIAM J. Imag. Sci. 7 (3) (2014) 1624–1644.
[54] T. Mertens, J. Kautz, F.V. Reeth, Exposure Fusion. in 15th Pacific Conference on Computer Graphics and Applications (PG'07), 2007.
[55] B.S. Richards, D.P.S. CapÃo, A.I. SchÄfer, Renewable energy powered membrane technology. 2. The effect of energy fluctuations on performance of a photovoltaic hybrid membrane system, Environ. Sci. Tech. 42 (12) (2008) 4563–4569.
[56] A.B. Schäfer, Richards, Renewable energy powered membrane technology. 1. Development and characterization of a photovoltaic hybrid membrane system, Environ. Sci. Tech. 41 (3) (2007) 998–1003.
[57] F.M. Savoy, S. Dev, Y.H. Lee, S. Winkler. Geo-referencing and stereo calibration of ground-based Whole Sky Imagers using the sun trajectory. IEEE.
[58] Q. Li, W. Lu, J. Yang, A hybrid thresholding algorithm for cloud detection on ground-based color images, J. Atmos. Oceanic Tech. 28 (10) (2011) 1286–1296.
[59] P. Pawar, C. Cortés, K. Murray, J. Kleissl, Detecting clear sky images, Sol. Energy 183 (2019) 50–56.
[60] C.N. Long, J.M. Sabburg, J. Calbó, D. Pagès, Retrieving cloud characteristics from ground-based daytime color all-sky images, J. Atmos. Oceanic Tech. 23 (5) (2006) 633–652.

[61] M.S. Ghonima, B. Urquhart, C.W. Chow, J.E. Shields, A. Cazorla, J. Kleissl, A method for cloud detection and opacity classification based on ground based sky imagery, Atmos. Meas. Tech., 5 (11) (2012) 2881–2892.
[62] R. Barzegar, M.T. Aalami, J. Adamowski, Coupling a hybrid CNN-LSTM deep learning model with a boundary corrected maximal overlap discrete wavelet transform for multiscale lake water level forecasting, J. Hydrol. 598 (2021) 126196.
[63] Y. Lecun, Y. Bengio, G. Hinton, Deep learning, Nature 521 (7553) (2015) 436–444.
[64] A. Khan, A. Sohail, U. Zahoora, A.S. Qureshi, A survey of the recent architectures of deep convolutional neural networks, Artif. Intell. Rev. 53 (8) (2020) 5455–5516.
[65] R.A. Rajagukguk, R.A.A. Ramadhan, H.-J. Lee, A review on deep learning models for forecasting time series data of solar irradiance and photovoltaic power, Energies 13 (24) (2020) 6623.
[66] S. Hochreiter, J. Schmidhuber, Long short-term memory, Neural Comput 9 (8) (1997) 1735–1780.
[67] M. Aslam, K.H. Seung, S. Jae Lee, J.-M. Lee, S. Hong, E.H. Lee, Long-term Solar Radiation Forecasting using a Deep Learning Approach-GRUs. IEEE.
[68] T.E. Hoff, R. Perez, J. Kleissl, D. Renne, J. Stein, Reporting of irradiance modeling relative prediction errors, Prog. Photovolt. Res. Appl. 21 (7) (2013) 1514–1519.
[69] M. Paulescu, E. Paulescu, Short-term forecasting of solar irradiance, Renew. Energy 143 (2019) 985–994.
[70] M. Diagne, M. David, P. Lauret, J. Boland, N. Schmutz, Review of solar irradiance forecasting methods and a proposition for small-scale insular grids, Renew. Sustain. Energy Rev. 27 (2013) 65–76.
[71] C. Feng, J. Zhang, W. Zhang, B.-M. Hodge, Convolutional neural networks for intra-hour solar forecasting based on sky image sequences, Appl. Energy 310 (2022) 118438.